SUPPRESSION OF HIGH TRANSVERSE MOMENTUM CHARGED HADRONS IN AU+AU
COLLISIONS AT 200 GEV NUCLEON-NUCLEON CENTER OF MASS ENERGY

by

JASON BRYSLAWSKYJ

A dissertation submitted to the Graduate Faculty in Physics in partial fulfillment of the
requirements for the degree of Doctor of Philosophy, The City University of New York

2016

This manuscript has been read and accepted by the Graduate Faculty in Physics in satisfaction of the dissertation requirement for the degree of Doctor of Philosophy.

Professor Stefan Bathe

_____   _____

Date   Chair of Examining Committee

Professor Igor Kuskovsky

_____   _____

Date   Executive Officer

Professor Jiangyong Jia
Professor Peter Orland
Professor Adrian Dumitru
Professor Brian Tiburzi
Supervisory Committee

THE CITY UNIVERSITY OF NEW YORK

Abstract

Suppression of High Transverse Momentum Charged Hadrons in Au+Au Collisions at 200 GeV Nucleon-Nucleon Center of Mass Energy

by

Jason Bryslawskyj

Abstract

The dynamical properties of quark gluon plasma are studied in heavy ion collisions. Gold ions are accelerated with the Relativistic Heavy Ion Collider (RHIC) at Brookhaven National Laboratory and collided at energies up to 200 GeV per nucleon. Collision products and their properties are detected and measured with the PHENIX detector. At these energies the colliding ions may form a thermalized distribution of quarks and gluons called the Quark-Gluon Plasma. The suppression of single hadrons still provides one of the strongest constraints on energy loss mechanisms in the Quark-Gluon Plasma. Presently, neutral pions provide the best measurement at RHIC of single particle suppression. Charged hadrons have independent sources of systematic uncertainty and can thus provide additional constraints. Background from off-vertex sources such as photon conversions and weak decays, which mimic high p_T particles, have limited the measurement of charged hadrons to $p_T < 10$ GeV/c at PHENIX. The newly installed silicon vertex tracker upgrade (VTX) can reject this background allowing the measurement of the charged hadron spectrum out to a significantly higher momentum, up to 26 GeV/c. The VTX is capable of performing precision measurements of the distance of closest approach of a track to the primary vertex (DCA). Off-vertex photon conversions and weak decays are vetoed with the VTX by rejecting tracks with large DCA.

Thesis Supervisor: Stefan Bathe
Title: Professor, Department of Natural Sciences

Acknowledgments

For Kaylie

Die Welt ist die Gesamtheit der Tatsachen, nicht der Dinge.

Wittgenstein

Contents

List of Figures

List of Tables

Chapter 1

Introduction

1.1 Motivation

For the last millenia, man has been probing deeper and deeper to find the most fundamental causes of physical phenomena. From our present understanding these causes can be reduced to several fundamental interactions. Among them are gravitational interactions, electroweak interactions and strong interactions governed by Quantum Chromodynamics (QCD). Our investigations of these interactions have led us to uncover the very form in which matter is organized. Discovering molecules, atoms and finally their constituent subatomic particles. Over the centuries, our knowledge of the fundamental forces has grown considerably, but our understanding of the fundamental QCD interactions in particular is still just beginning.

Experiments involving high energy collisions explore these nuclear forces by accelerating and colliding particles at energies where these nuclear forces dominate the interaction. At the Relativistic heavy Ion Collider (RHIC) at Brookhaven National Laboratory, such heavy ion collisions are performed. These ions are from atoms such as gold that contain a large number of neutrons and protons. Gold atoms are stripped of their electrons so that the large positive charge of their nuclei can be used to accelerate them up to nearly the speed of

light. Two 2.4 mile rings of superconducting magnets contain beams of these ions moving in opposite directions. At six locations on the rings, the beams are allowed to collide. If two gold ions collide with enough energy they may form a quark-gluon plasma. The quark-gluon plasma is a novel state of matter in which quarks are deconfined allowing them to move freely in a thermalized state. Since at low energies, in everyday matter for instance, quarks are confined, bound together in pairs or triplets, studying them at high energies where they are deconfined will allow us deeper insight into the nuclear forces that govern their behavior.

To study the properties of the quark-gluon plasma, the properties of particles that are produced during these high energy collisions at RHIC are studied. These particles are detected at two large experiments PHENIX and STAR. PHENIX or Pioneering High Energy Nuclear Interactions is a system of detectors which sits at one of the intersection points of the two colliding beams. 4,000 tons of detecting equipment allows the trajectory, momentum and energy of resulting particles created in these collisions to be measured. With this information the properties of the quark-gluon plasma itself can be deduced and more is learned about the quark-gluon plasma.

An upgrade to the PHENIX experiment, the silicon vertex tracker or VTX allows decay products to be resolved even closer to the event vertex. The VTX is a barrel shaped array of micropattern silicon sensors that surround the collision point at very close proximity. As particles created in the collision pass through the sensors, their trajectory can be reconstructed to a much greater resolution than was before possible.

1.2   High p_T Charged Hadrons

The nuclear interactions occurring during a heavy ion collision can be roughly divided into two types, hard scatterings of the ion's constituent partons in the initial stages of the collision and soft scatterings of the partons in the medium. Collision products originating from the

soft scatterings provide information about the thermodynamic properties of the medium. Products from hard scatterings initially carry the energy and momentum transferred during the scattering, but lose energy and momentum as they traverse the strongly interacting quark-gluon plasma. Measuring the energy and momentum loss of these hard probes is thus a measurement of the dynamical properties of the medium itself.

This analysis studies the suppression of charged hadrons at large transverse momentum, p_T, the vector component of the momentum in the plane perpendicular to the colliding beam. Whereas the longitudinal momenta of produced particles largely originates from the beam itself, the transverse momentum is generated by particle interactions during the collision. High p_T charged hadrons originate from hard scatterings of constituent quarks at large momentum transfer. The modification of the p_T spectrum of charged hadrons caused by interactions with the medium are measured by comparing the spectrum obtained from central Au+Au collision to that obtained in peripheral collisions where the probability of a plasma forming is drastically decreased.

1.3   Energy Loss

As will be seen below, the momentum spectrum of charged hadrons is a steeply falling spectrum. This makes the p_T spectrum highly sensitive to small losses in momenta which result in large reductions in yield. The primary energy loss mechanism for partons traversing the strongly interacting medium is due to gluon radiation. Color charge centers in the plasma scatter the parton, inducing gluon Bremsstrahlung. Energy loss to Bremsstrahlung reduces the parton's momentum causing modification to the p_T spectrum. Consequently. an observation of a modification to the spectrum, is an observation of the color charge density of the plasma[6].

Several theoretical models of energy loss have been put forth to explain the interac-

tion of hard scattered collision products with the medium. In general, such a model must describe the hydrodynamics of the medium and then estimate from perturbative QCD calculations the modification of the fragmentation function of the the hard scattered parton. It is assumed that the final hadronic cross section is factorizable into components, namely the initial nuclear structure functions, initial state effects, the cross section of the initial hard scattering itself and lastly the final hadronic fragmentation function modified by the strongly interacting plasma[16]. Most recent models, attempt to describe the energy loss using a single free parameter $\langle \hat{q} \rangle$, the transverse momentum diffusion coefficient defined as the per mean free path average of the transverse momentum imparted to the parton by the medium squared[1],[23].

One such approach is the higher twist formulation. Here medium effects are modeled as higher order twist corrections to the cross section obtained from Deep-Inelastic Scattering (DIS). If one assumes that the parton jet energy E is much greater than its virtuality Q, itself much greater than the momentum scale of the medium, then the collinear approximation can be used[22],[16]. In this approximation, the modified fragmentation function is factorized from the hard scattering cross section. This allows the modified fragmentation function obtained from DIS to be applied to heavy-ion collisions. The higher twist approach appears to be appropriate in systems with a large Debye mass or with otherwise short color correlation lengths. It fails when jet energies become large enough to become effected by gluon saturation, but these energies are believed to be higher than what is obtainable at RHIC[16].

Another possibility is to model the quark-gluon plasma as many Debye screened color charges separated enough that the color screening length is much smaller than the partonic probe's mean free path. The energy loss due to multiple scattering off of these color charges can be calculated by a path integral over a path-ordered non-abelian Wilson line[31],[16]. This is done in the Armesto-Salgado-Wiedemann (ASW) formalism. Additionally, this model

provides an intuitive definition of the opacity of the medium, $\bar{n} = L/\lambda$. Where λ is the mean free path of the jet and L is the thickness of the plasma. In this formalism, the propagation of the parton and the radiated gluon Bremsstrahlung can be expressed by the Dyson-Schwinger equation with an effective Green's function for the parton and the color potential of the medium[16]. This equation can be solved for by integrating the path ordered Wilson line. Each gluon emission is assumed to be causally independent and follows a Poisson distribution for the probability of the parton to lose a momentum fraction ΔE in n tries[28]:

$$P_n(\Delta E) = \frac{e^{-\langle I \rangle}}{n!} \Pi_{i=1}^n \left[\int d\omega_i \frac{dI}{d\omega_i} \right] \delta(\Delta E - \sum_{i=1}^n \omega_i) \tag{1.1}$$

for radiated gluon energies ω_i and where $\langle I \rangle$ is the average number of gluons radiated in an interaction with the medium. This probability can then be used to calculate the modification to the jet fragmentation function. As with the higher twist approach, the ASW model does not take into account any interactions with the medium which cause flavor changes[16].

An additional way of modeling the energy loss of a hard parton in the quark-gluon plasma is by modeling the plasma as a thick medium in thermal equilibrium with an asymptotically high temperature. As $T \to \infty$ the coupling constant $g \to 0$, because of asymptotic freedom[16]. This allows for a scale hierarchy in orders of g:

$$T \gg gT \gg g^2 T \tag{1.2}$$

An effective field theory can then be obtained by summing hard loops with $p \sim T$. This gives an effective theory of the soft modes $p \sim gT$. The parton is assumed to have an energy much larger than the medium temperature and interact softly with the plasma with momentum transfers of order gT[13]. This model is known as the Arnold-Moore-Yaffe (AMY) model. By letting the parton fragment in vacuum after leaving the medium, the modification to the

spectrum can be found after convolving the vacuum fragmentation functions with the parton distributions. This formulation, however, results in a different estimate of the energy density of the medium than lattice QCD calculations. In addition, in this approach the coupling constant must be used as a parameter of the fit[16].

The suppression of high-p_T hadrons in heavy ion collisions has been estimated by each of these models. If all three models are constrained to use the same hydrodynamic model as the medium, the phenomenological differences in each approach's expectation of the modification of the hadron spectrum can be observed. This has been done [16], first by adjusting the value of $\langle \hat{q}_0 \rangle$ (the maximum value of $\langle \hat{q} \rangle$) in each model, until they agree with the centrality dependence of the suppression of neutral pions as measured by PHENIX [29]. Although this produces a different value of $\langle \hat{q} \rangle$ for each model[1] the p_T dependence of the hadron suppression appears to be consistent with PHENIX data and appears to be almost constant with p_T, with a slight upwards slope[16].

_____

[1]The higher twist model gives a $\langle \hat{q}_0 \rangle$ of 4.3 GeV^2/fm, 4.1 GeV^2/fm for AMY and the ASW approach gives a $\langle \hat{q}_0 \rangle$ of 18.5 GeV^2/fm[16].

1.4 Previous Measurements

The previous measurement of charged hadron suppression at PHENIX was limited in p_T reach by off-vertex background tracks. At PHENIX, the measurement of momentum assumes that tracks originate from the collision vertex. For the vast majority of reconstructed particles, this assumption holds and these particles are reconstructed with the correct momentum. However, the vast majority of particles are also low p_T particles from the collision vertex. Off-vertex low p_T particles such as electrons from photon conversions and secondary products of weak decays, can be misreconstructed with an arbitrarily large momentum. At low p_T these sources of background are negligible, but because of the steeply falling p_T spectrum at high p_T these background particles begin to compete with the signal. These misreconstructed background tracks dominate the spectrum above $p_T > 6\,\mathrm{GeV/c}$ and limited the measurement of charged hadrons to $p_T < 10\,\mathrm{GeV/c}$ when only using central arm detectors[8]. The published fully corrected spectra of charged hadron tracks is shown in figure 1-1. The p_T reach of the charged spectrum will be improved in this analysis by using the Silicon Vertex Tracker Upgrade, installed in 2011, to reject off-vertex background.

A similar measurement has been made by PHENIX of high p_T neutral pions. As shown in figure 1-2, the spectrum of neutral pions has been measured out to much higher p_T. Although the π^0s have been measured up to 19 GeV/c, the charged hadron spectrum provides an important complimentary measurement. The π^0 measurement has different sources of systematic errors than the charged hadron measurement. After significant background reduction by the silicon vertex tracker, the main source of systematic uncertainty in the charged hadron measurement comes from the resolution of the momentum measurement by the drift chamber, which increases with p_T. The π^0s on the other hand are limited at high p_T by shower merging in the electromagnetic calorimeter. A complimentary charged hadron measurement would also allow the comparison of the suppression of π^0 mesons to a
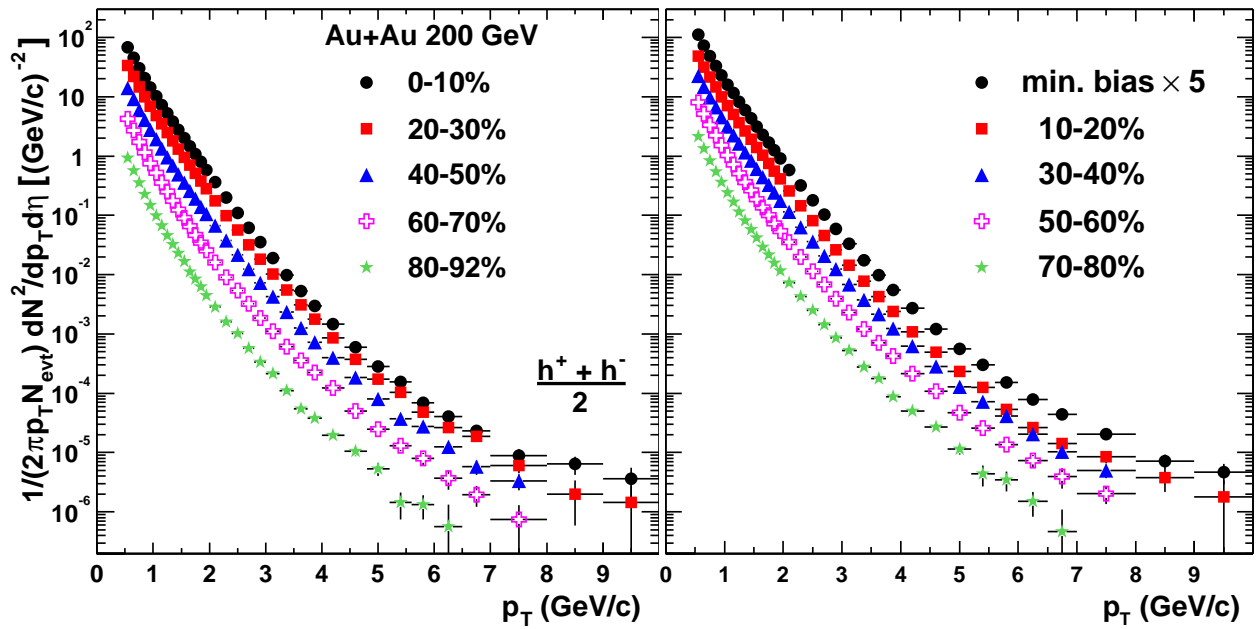
Figure 1-1: Published charged hadron invariant yield as measured by PHENIX for several centralities [8].

combination of mesons and baryons.
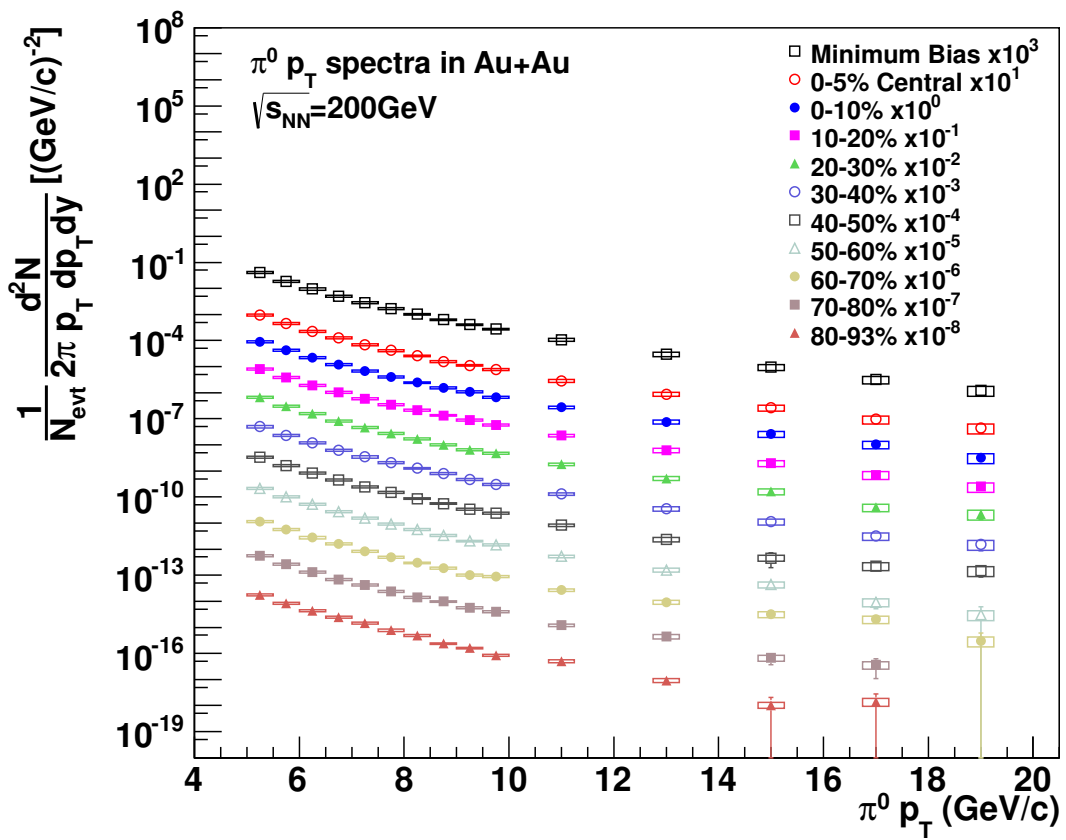
Figure 1-2: Published invariant yield of neutral pions as measured by PHENIX for several centralities. [2]

Chapter 2

Experiment
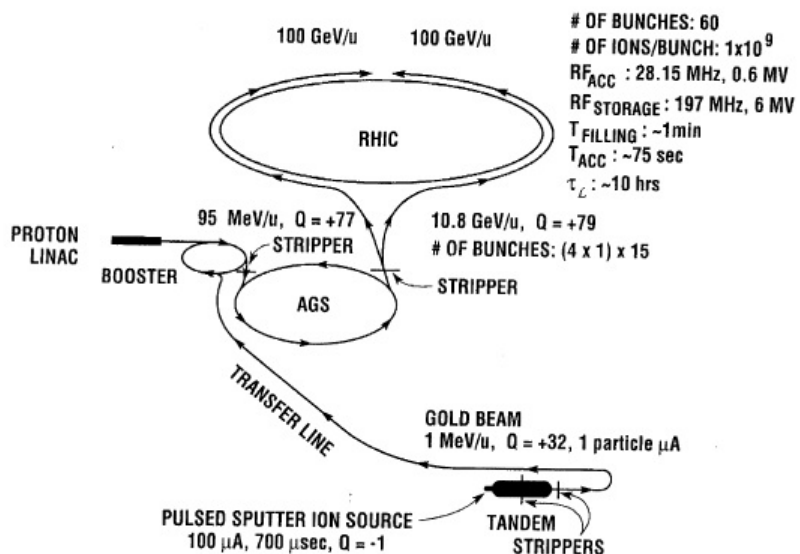
Figure 2-1: Schematic of the RHIC accelerator. [21].

My analysis will focus on measurements performed using the PHENIX experiment. The PHENIX experiment is one of two operational detectors at RHIC, the Relativistic Heavy Ion Collider at Brookhaven National Laboratory. Shown diagrammatically in figure 2-1, the RHIC accelerator consists of 2 independent storage rings of superconducting magnets each 3.8 km in circumference. RHIC is capable of accelerating heavy ions, such as Au for example,

to energies of 100 GeV per nucleon and accelerating protons to 250 GeV. Independent storage rings allow different ion species to be collided, allowing the collision geometry to be varied. For example, in the past deuterium has been collided with gold to study a smaller colliding system. Similarly, uranium nuclei have been collided together to study the effect of varying the elliptical shape of the colliding system.

At RHIC, gold ions start at the Electron Beam Ion Source or (EBIS) which acts as an injector, accelerating ions to low energies from rest. At the time data was taken for this analysis, the injector for RHIC was a Tandem Van de Graff generator as depicted in figure 2-1. The Tandem Van de Graff generator accelerates gold ions to energies of 1 MeV per nucleon. They are then transferred to the booster accelerator which passes them to the Alternating Gradient Synchrotron (AGS) at 95 MeV per nucleon and strips them of most of their electrons. The AGS accelerates the ions to 10.8 GeV per nucleon before injecting them into the main RHIC rings. Beams from each ring criss cross at six intersection points and are steered to collide at two of these points. At these points lie the detector experiments PHENIX and STAR.

2.1 PHENIX

The PHENIX or Pioneering High Energy Nuclear Interactions Experiment detector is comprised of many different subdetectors. Each subdetector is designed to measure particular dynamical properties of the collision products. My analysis involved a subset of the available detectors in the PHENIX experiment. The internal design and physics capabilities of those detectors will be discussed in the following sections. Specifically, the following detectors were used: the Beam-Beam Counters (BBC), the silicon vertex tracker (VTX), the Drift Chambers (DC), the Pad Chambers (PC1,PC3) and the Electromagnetic Calorimeter (EMC). Figure 2-2 depicts a quarter cut out of the PHENIX detector. The PHENIX subdetectors
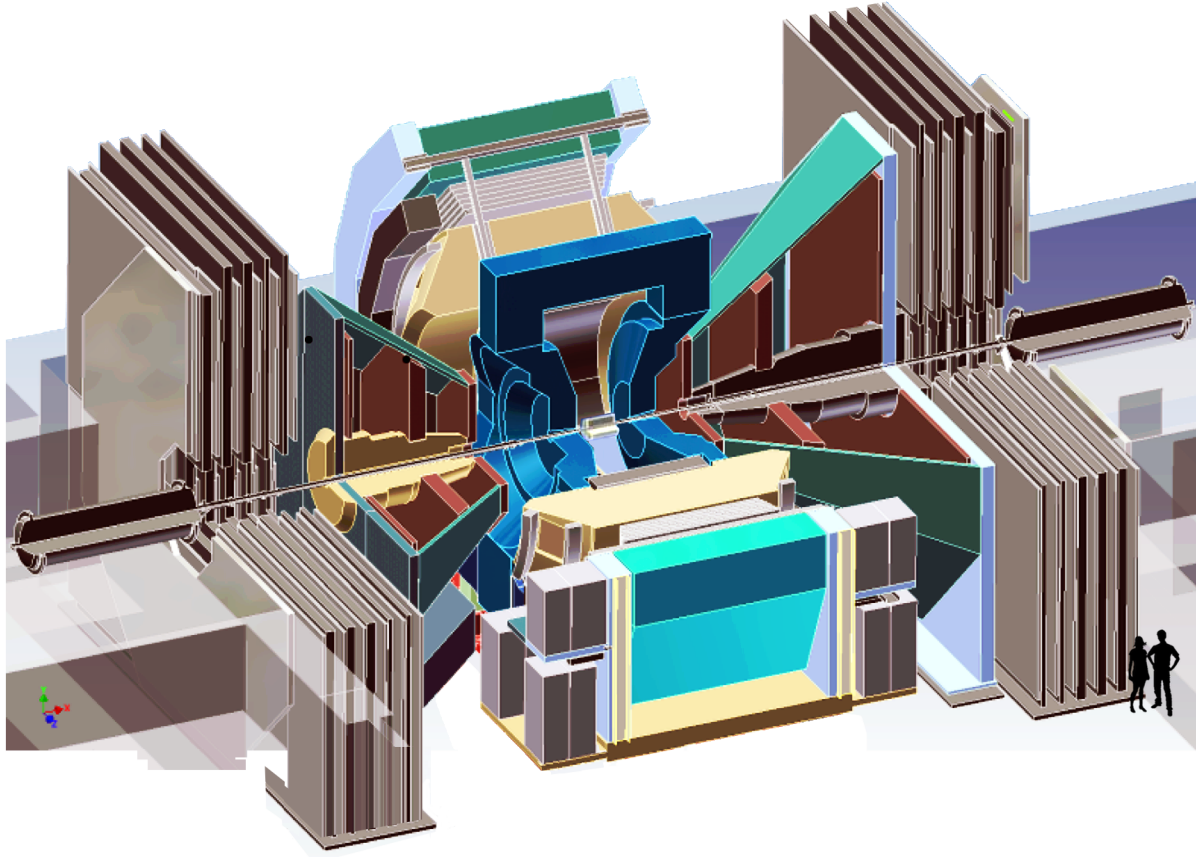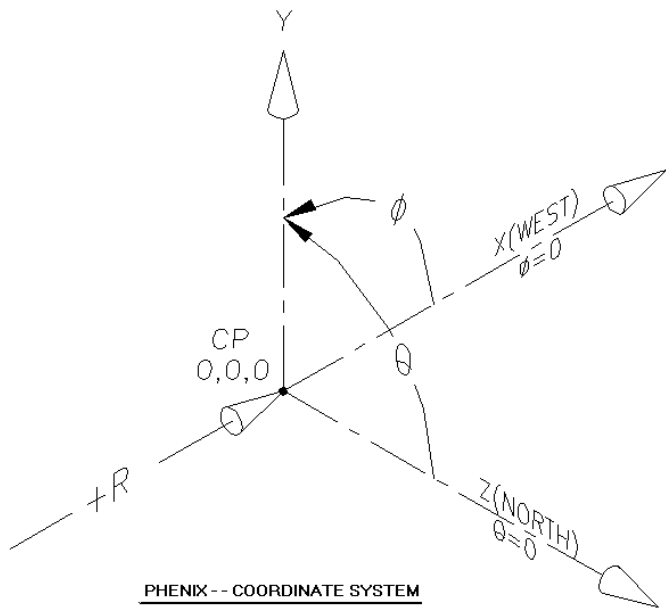
Figure 2-2: Cut out of the PHENIX detector from above and orthogonal to the beam direction. [30].

are roughly organized around 3 regions of pseudorapidity (see below). At very large pseudorapidity ($3.0 < \eta < 3.9$), are placed detectors such as the Beam-Beam Counters, which detect collision products that scatter at very large angles. At large pseudorapidity ($1.2 \gtrsim \eta \gtrsim 2.2$), the muon arm detectors are placed. Finally, at midrapidity ($-0.35 < \eta < 0.35$) are the central arm tracking detectors. This analysis will study the spectrum of charged hadrons at midrapidity and will therefore mostly involve the central arm tracking detectors and will use the BBC to characterize events.

2.1.1 PHENIX Coordinate System

The 3 dimensional coordinate system depicted in figure2-3 will be used throughout. Here the z axis is placed along the beam axis. ϕ wraps around from 0 to 2π in the plane orthogonal to z starting with $\phi = 0$ on the x axis. θ is defined in the $y - z$ plane starting with $\theta = 0$ at the z axis, to $\theta = \pi$ at the y axis.

Figure 2-3: PHENIX coordinate system. The z axis is placed along the beam axis and the x axis faces east to west [18].

2.1.2 Pseudorapidity

The solid angle acceptance of each of the PHENIX subdetectors is defined in terms of pseudorapidity (η). Pseudorapidity is an approximation of rapidity (y):

$$y = \frac{1}{2} \ln \left(\frac{E + p_z}{E - p_z} \right) \tag{2.1}$$

When $p \gg m$, y can be expanded:

$$y = \frac{1}{2} \ln \frac{\cos^2(\theta/2) + m^2/4p^2 + ...}{\sin^2(\theta/2) + m^2/4p^2 + ...} \tag{2.2}$$

which itself can be approximated as

$$\eta \equiv -\ln \tan(\theta/2) \tag{2.3}$$

where η is defined as the pseudorapidity, and is a convenient transformation of the polar angle θ [25].

2.1.3 Beam Beam Counters (BBC)

The beam beam counters are Cherenkov counters placed around the beam pipe at very large pseudorapidity $(3.0 < \eta < 3.9)$ and positioned down the beam pipe at $z = \pm 1.44$ m. The main functions of the BBC for this analysis are to trigger the data acquisition system on heavy ion collisions, to exclude collisions which take place too far from the center of the PHENIX acceptance and to measure event centrality by measuring collision multiplicity. The BBCs are comprised of 64 quartz Cherenkov radiators coupled to photomultiplier tubes (PMTs). As high energy particles pass through the quartz, they travel faster than the speed of light in the material, creating Cherenkov radiation which is detected by the photomultiplier

tubes. On average, for a central Au+Au event, 15 particles are expected to pass through each counter. [11]

The BBCs can determine whether or not a collision has taken place by detecting collision products that have scattered at large angles. By counting the number of products, a measurement of the collision's multiplicity can be made, from which the collision's centrality is inferred. The measurement of centrality will be discussed in greater detail below. The BBC can also provide a measurement of the z vertex position. This is performed by triggering on coincidences between the north and south BBCs and measuring the difference in time.[11] For this analysis, however, the silicon vertex detector (VTX) was used to measure the z vertex position, as it can more accurately measure the vertex position.
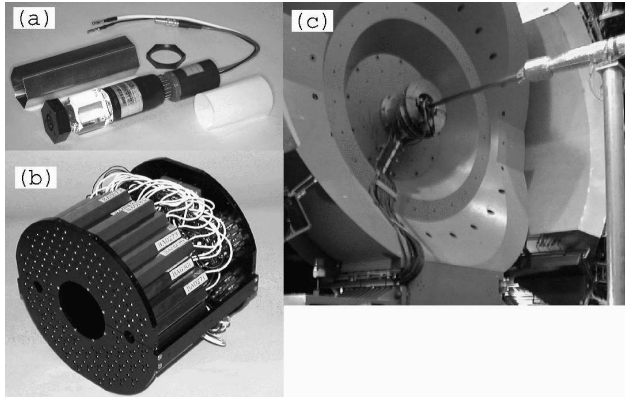
Figure 2-4: BBC detector. (a) Individual Cherenkov radiator with attached (b) An entire BBC with the Cherenkov radiators exposed. (c) The BBC as positioned in PHENIX[11].

2.1.4 PHENIX Magnets

As shown in figure 2-5, the PHENIX experiment has a magnet system consisting of two coils (inner and outer) in the central arm region and north and south magnets for the muon arms. The purpose of the PHENIX magnet system is to bend the trajectories of charged particle via the Lorentz force, and subsequently measure the bend thereby measuring the

particle's momentum. Here, we will concern ourselves with only the central arm magnet as this analysis only studies midrapidity particles.
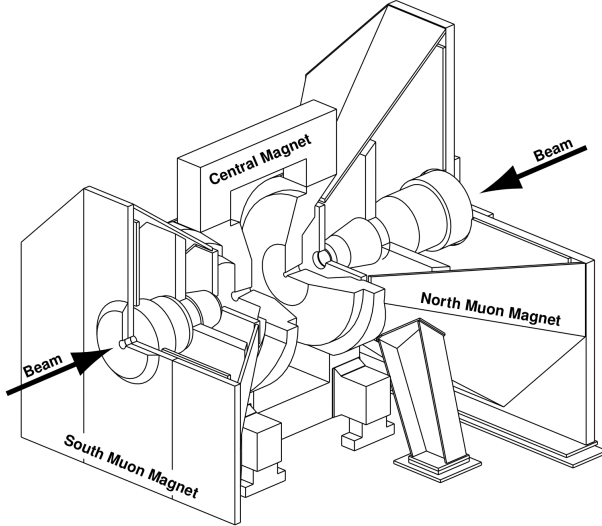
Figure 2-5: The PHENIX magnet system[14].

The PHENIX central arm magnet consists of two coils. When both are operating simultaneously, as in this analysis, they provide a field integral ranging form $0.43 - 1.15$ T·m. The magnetic field covers the same pseudorapidity as the PHENIX central arms $(-0.35 < \eta < 0.35)$ and covers a polar angle of $70° < \Theta < 110°$ [14]. The central arm magnet is an axial magnet providing a very uniform pointing in the direction parallel to the beam axis ($\hat{z}$). The axial field changes the momentum of moving charged particles in the plane perpendicular, giving it a transverse momentum kick of:

$$\Delta P_{\hat{\phi}} = -q \int B dz \qquad (2.4)$$

2.1.5   Silicon Vertex Tracker (VTX)

The innermost subdetector of PHENIX's midrapidity central arms is the silicon vertex tracking detector or VTX. The VTX consists of four layers of micropattern silicon detectors placed

16

close to the beam pipe. The VTX was installed in PHENIX in 2011 with the purpose of using precision silicon detectors close to the collision point in order to accurately measure the collision vertex. Having a precise measurement of the collision vertex is crucial in improving tracking and background rejection.

As shown in the right panel of figure 2-6, the layers of the VTX form concentric cylindrical barrels very close to the beam pipe. Layers are labeled B0-B3, with the center radius of B0 positioned 2.63 cm from the average beam center and B3 positioned at 16.69 cm. The dimensions of all layers are given in table 2.1. The two innermost layers of the VTX are made of silicon pixel detectors and the outermost layers are composed of strippixel detectors. Pixel layers are made up of silicon "pixels", 50 μm x 425 μm rectangles of n type silicon with p^+ implants. These pixels form diodes which are placed under a reverse bias. As a charged particle passes through the pixel, electron hole pairs are created, generating a current across the diode. Strippixel layers are made up of 80 μm by 3 cm "strippixels". A schematic diagram of a section of the strippixel detector is shown in figure 2-7. As the strippixel layers are placed at larger radius than the pixel detectors, they must cover a larger cross-sectional area. To cover a larger area, the strippixels are made up of criss-crossing horizontal and diagonal silicon strips. This gives an effective sensitive area of 80 μm x 1000 μm. The VTX covers a pseudorapidity $|\eta| < 1.2$ and an azimuthal angle of $\Delta\phi \sim 2\pi$.

2.1.6 Drift Chamber

After the VTX, midrapidity tracks encounter the PHENIX drift chamber (DC). The drift chamber is a tracking detector consisting of a large multiwire chamber filled with 50% Ar and 50% C_2H_6. As charged particles pass through the DC, they ionize the gas and the freed electrons drift towards the DC's anode's wires. Combining the measured drift time with the postion of the wires allows the path of the charged particle traveling through the DC to be
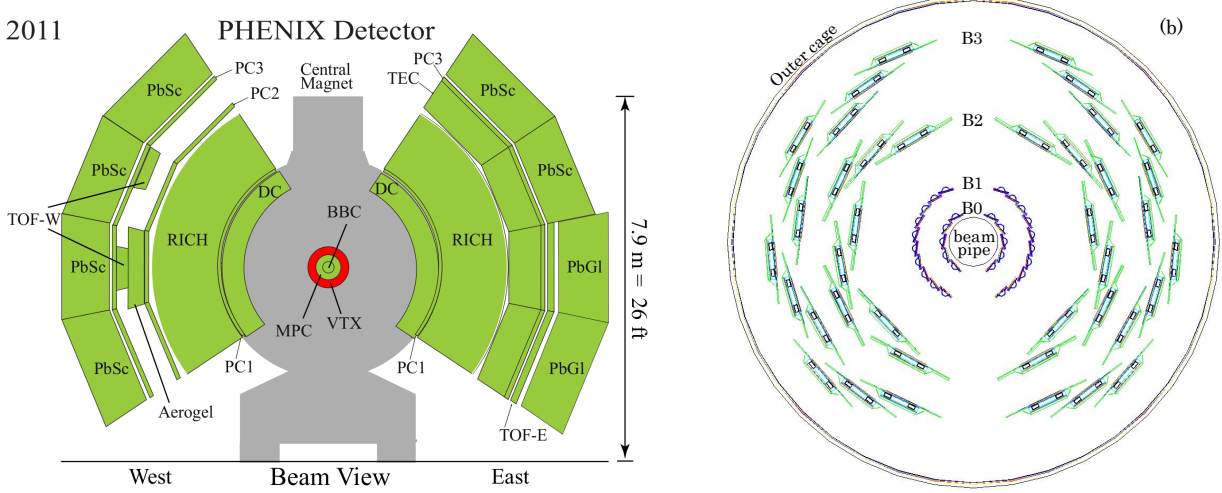
Figure 2-6: Left: Cross section of the PHENIX central arm detectors with the VTX detector. Right: Cross section of VTX detector[4].

reconstructed.

The DC covers a pseudorapidity $|\eta| < 0.35$ and an azimuthal angle of $\Delta\phi \sim 2\pi$. Its position in PHENIX is depicted in figure 2-6 and the DC itself is shown in more detail in figure 2-8. It provides an angular (ϕ) resolution of 1 mrad and a longitudinal (z) resolution of 2 mm[5].

In this analysis, the drift chamber provides the primary measurement of each track's transverse momentum. As track trajectories are bent by the PHENIX central magnet they enter the drift chamber at an angle. As shown in figure 2-9 the drift chamber measures transverse momentum by measuring the angle α between a track's path in the drift chamber and a straight line projection back to the collision vertex. From α, the transverse momentum p_T can be calculated:

$$p_T = \frac{84 \text{ mrad}}{\alpha} \tag{2.5}$$

where 84 mrad is the integral of the PHENIX central arm magnetic field [15]. The transverse momentum resolution is limited by the drift chamber's angular resolution and
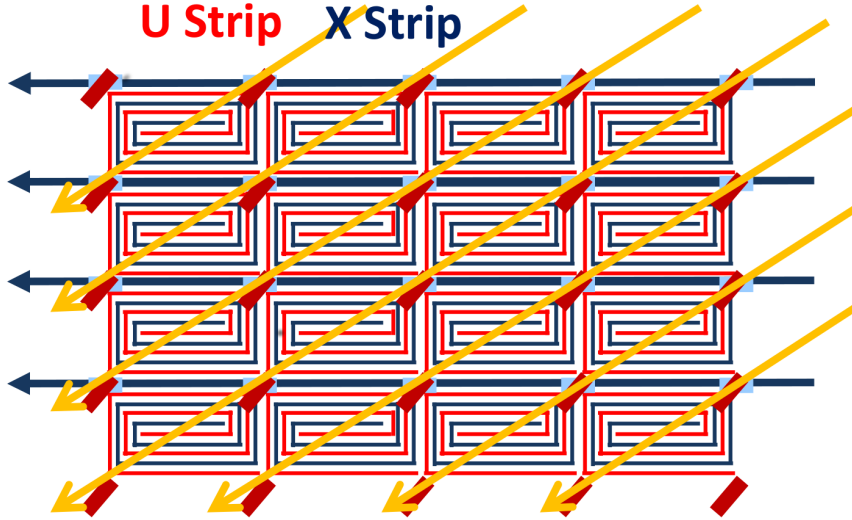
Figure 2-7: Diagram of a 4x4 section of the strippixel detector[19].

multiple scattering and has been measured to be [9]:

$$\frac{\delta p}{p} = 0.7\% \oplus 1.0\% \times p(\text{GeV/c}) \qquad (2.6)$$

2.1.7 Pad Chambers

One method of improving the correct identification of tracks as particles and reconstruction of particle trajectories, is to install additional tracking layers. To this end, pad chamber detectors (PC1) are placed directly behind the drift chamber, behind the RICH on the west arm (PC2) and directly in front of the electromagnetic calorimeter (PC3).

Pad chamber detectors are multiwire gas vessels, which detect charged particles via ionization similar to the drift chamber. The pad chambers, however are thin chambers with a high density of wires in the planes parallel to $\hat{\phi}$. They function, therefore, not to provide angular information but additional points for the tracking procedure. Tracks found in the drift chamber are projected on to the pad chambers, and if no hits are found in the PC in

Layer	0	1	2	3
Nominal Radius (cm)	2.63	5.13	11.77	16.69
# of Ladders	10	20	16	24
Ladder Length (cm)	22.8	22.8	31.8	38.2
# of Sensors per Ladder	4	4	5	6
Sensor Dimensions (ϕ cm x z cm x d μm)	1.5 x 5.672 x 200	1.5 x 5.672 x 200	3.49 x 6.37 x 625	3.49 x 6.37 x 625
Active Area (ϕ cm x z cm)	1.28 x 5.56	1.28 x 5.56	3.072 x 6.000	3.072 x 6.000
# of Chips per Sensor	4	4	12	12
# of Channels per Chip	8192	8192	128 x 8 bits	128 x 8 bits
# of Pixels per Chip	256 x 32	256 x 32	384 x 2(X/U) x 2	384 x 2(X/U) x 2
Pixel Dimensions (ϕ μm x z μm)	50 x 425	50 x 425	80 x 3.0 (cm)	80 x 3.0 (cm)

Table 2.1: Hardware specifications of the silicon vertex tracking detector (VTX).

the vicinity of the track projection, the track can be rejected as background. PC1 and PC3 cover the same solid angle as the drift chamber [5]. This analysis uses PC1 and PC3 in this way to reject backgrounds. The PC2 was not used, as it would have required either halving the acceptance or introducing an east-west asymmetry into the efficiency.

2.1.8 Electromagnetic Calorimeter

The outermost subdetector in the PHENIX central arms is the electromagnetic calorimeter (EMC or EmCal). As shown in figure 2-6, there are two types of electromagnetic calorimeters used in PHENIX. In the west arm, the calorimeter is split into four sectors of lead scintillator PbSc and in the east arm, there are 2 sectors of lead scintillator and 2 sectors of lead glass PbGl. Both types of detector use a combination of pair production and Bremsstrahlung to detect electrons and photons. The lead scintillator is a sampling type calorimeter [12]. It is composed of alternating tiles of lead and scintillator. When a high energy electron enters a lead tile, it scatters off the charges in the lead thereby bending its path and accelerating. An accelerating charge undergoes Bremsstrahlung, emitting photons. These photons may then undergo pair production, where they decay into electron-positron pairs. The produced
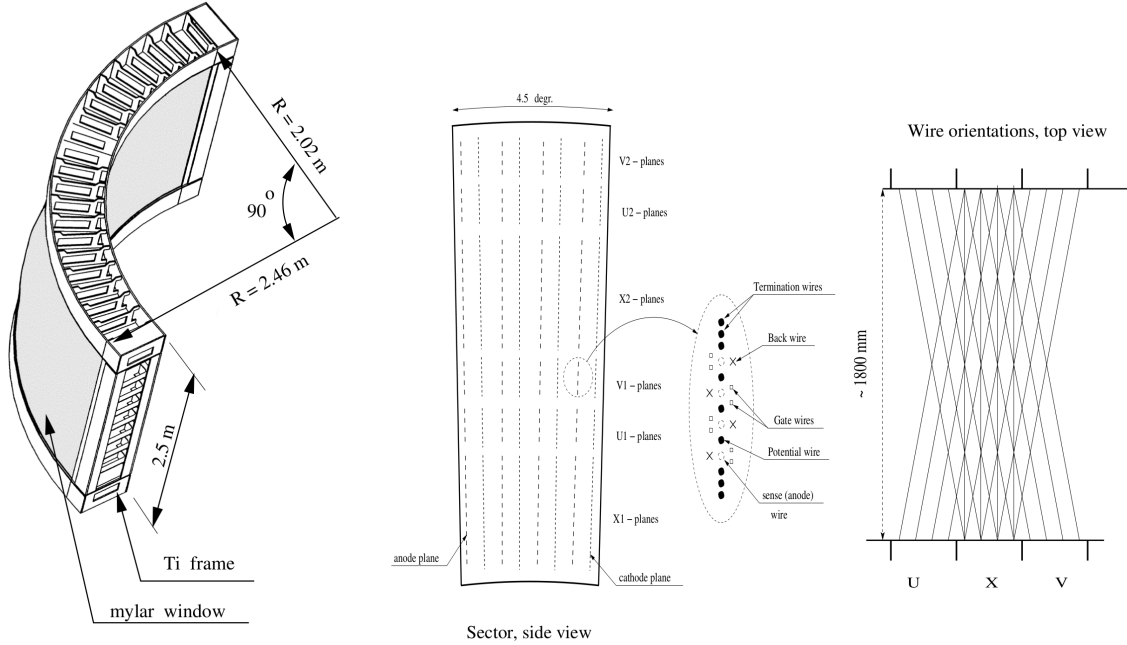
Figure 2-8: Left: Cross-section of one half of the drift chamber. Right: Schematic of the inside of one DC sector[5].

electron or position will then undergo Bremsstrahlung, emitting more photons, which themselves may undergo pair production creating a chain of electron-photon generation called an electromagnetic shower. A shower in the EmCal need not start with a high energy electron, but may start with a photon that undergoes pair production. Hadrons can also be detected, as long as they undergo a so called hadronic shower. Hadrons may interact with the dense detector material and produce additional hadrons through the strong interaction. If these produced hadrons have a high enough energy they will also interact with the detector material.

In the lead scintillator, the electrons in an electromagnetic shower scintillate as they traverse the scintillator tiles. The produced scintillation light is transmitted via fibers to PMTs which count then number of photons. The lead glass detector, on the other hand is made from light permeable lead crystal. The crystal has a high enough charge density for high energy particles to initiate electromagnetic showers. The high index of refraction of the

21
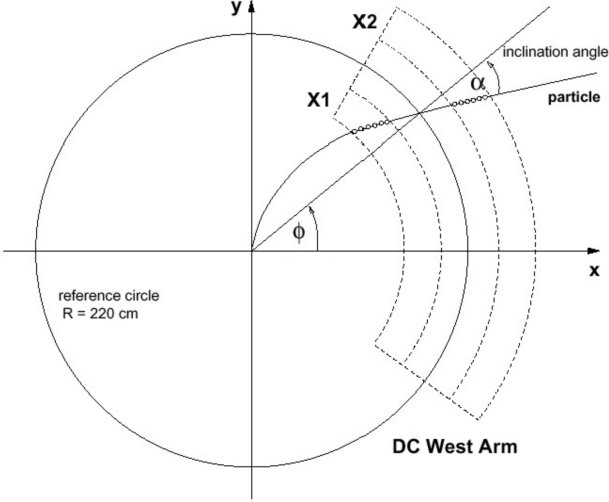
Figure 2-9: Schematic of a particle trajectory through the drift chamber. The drift chamber measures transverse momentum by measuring the angle between the track's path and a straight line projection to the collision vertex[17].

lead crystal allows the shower electrons to travel faster than the speed of light in the crystal, producing Cherenkov radiation. This Cherenkov light travels through the crystal and is read out by PMTs.

The energy resolution of the PbSc is [12]:

$$\frac{\sigma(E)}{E} = \frac{8.1\%}{\sqrt{E(GeV)}} \oplus 2.1\% \tag{2.7}$$

and the energy resolution of the PbGl is [12]:

$$\frac{\sigma(E)}{E} = \frac{[5.9 \pm 0.1]\%}{\sqrt{E/GeV}} \oplus [0.8 \pm 0.1]\% \tag{2.8}$$

The lead scintillator sections of the EmCal are 18 radiation lengths long and 0.85 nuclear interaction lengths long. Likewise, the lead glass sections are 14.3 radiation lengths long and 1.05 nuclear interaction lengths long [12]. Therefore, there is a much higher probability for an electron or a photon to deposit the entirety of its energy in the EmCal than for a

22
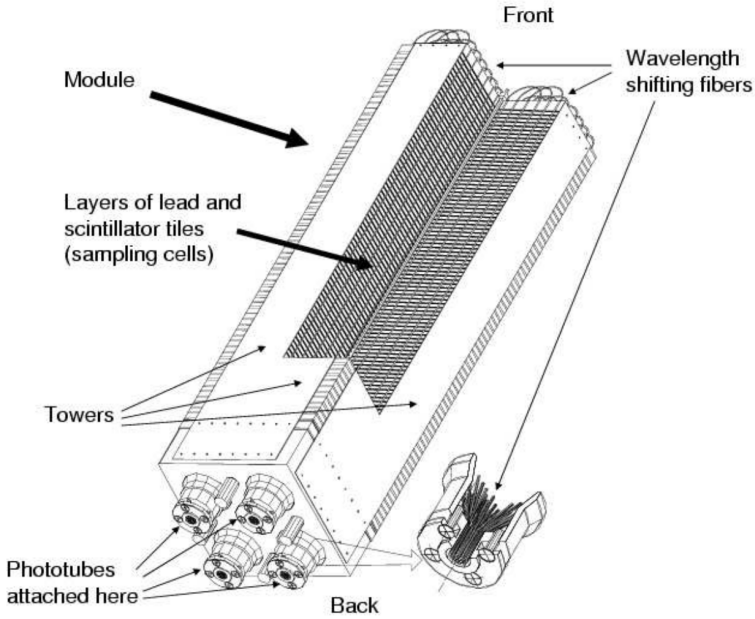
Figure 2-10: Cutout of a section of the electromagnetic calorimeter[12].

hadron. This limits the ability of the EmCal in measuring the energy of hadrons. However, even hadrons which do not deposit all of their energy are still detected and their position in the EmCal can be measured. In this analysis the EmCal is used as a final tracking point. Central arm tracks, which have had matching hits in the VTX, DC and PC are projected onto the EmCal. Such tracks are rejected, unless a matching hit in the EmCal is found.

Chapter 3

Analysis Cuts

3.1 Introduction

The main constraint on measuring the charged hadron spectrum is the background from sources which do not originate from the primary vertex. Particle momenta are measured using the PHENIX drift chamber. As the drift chamber measures momentum assuming that tracks originate from the primary vertex, off-vertex conversion electrons and secondary particles from weak decays can be misreconstructed as high p_T charged hadrons. To increase the signal to background ratio, drift chamber tracks are matched to other detectors in the PHENIX central arm. A candidate track must have triggered multiple wires in the drift chamber, and be matched to hits in the VTX, PC1, PC3 and the EmCal. This is done by projecting the trajectory of the track into each detector and looking for nearby hits. The exact criteria for accepting a track as a charged hadron, including how close hits must be to the track projection, are described in the sections below.

3.2   Centrality

3.3   BBC Triggering

PHENIX triggers on collision events by using the BBC detectors. As described above, the BBCs are Cherenkov counters located a very high pseudorapidity ($3.0 < |\eta| < 3.9$) in the north and south ends of the PHENIX detector. In this analysis, events were triggered on a coincidence of the north and south BBCs.

3.4   Longitudinal Vertex Cut

Collisions occurring in the PHENIX detector are found along a very wide distribution of positions along the longitudinal axis. In fact, any event within $z < \pm 30$ cm can fire the BBC trigger condition described in the previous section. However, products from collisions which occur far from PHENIX's longitudinal center may see large variations in detector acceptance. For this reason, cuts are placed on the longitudinal position, the z-vertex. Before the installation of the VTX detector, the z-vertex was measured by the BBC detectors. When a coincidence is observed between the north and south BBCs, the difference in arrival time is translated into the difference in distance between the two detectors. With its micropattern silicon pixels positioned close to the beam pipe, the VTX detector can make a much more precise measurement of the vertex position. The vertex position is measured by first forming tracks with the VTX alone, known as standalone tracks. These standalone tracks are projected back towards the beam pipe, and the spacepoint closest to the convergence of the majority of standalone tracks is taken as the collision vertex. Whereas the BBCs can detect the z-vertex with a resolution of $\sigma_z = 0.6$ cm, the VTX can measure the z-vertex within 70 μm [4]. Only events which have a z-vertex less than ± 10 cm are considered in this analysis.

3.5 Central Arm Cuts

Tracks are sampled from SVX Central Tracks (SVXCNT), which are central arm tracks matched to hits in the VTX. Cuts are placed both on the central are track component as well as on the VTX hits. In this section, the cuts placed on the central arm detectors are described.

3.5.1 Drift Chamber

Cuts are made in the drift chamber on track quality and acceptance. The quality of a drift chamber track, is determined by the combination of stereo wires which have been triggered. The optimal quality is labeled "61" and signifies not only an optimal combination of stereo wires, but also a unique matching hit in pad chamber 1 (PC1). A quality of "31", has the same combination of stereo wires hit, but with an ambiguous signal in PC1. This analysis only uses tracks which have a drift chamber quality of 61 or 31. A cut is also place on "zed", the z position of a track as it passes through the middle of the drift chamber (with a radius of 220 cm from the beam center). The value of |zed| must be less than 75 cm in order for the track to see the full PHENIX acceptance.

DC:
quality = 31 || 64
-75 cm < zed < 75 cm

Table 3.1: Cuts on drift chamber (DC) variables.

3.5.2 Pad Chamber 1

PC1 is a pad chamber detector which sits in front (closer to the beam) of the drift chamber. All PHENIX central arm tracks are matched to PC1 as background rejection and because

PC1 has better longitudinal resolution than the drift chamber.

3.5.3 Pad Chamber 3

Pad chamber 3 (PC3) is a pad chamber detector positioned directly in front of the electro-magnetic calorimeter. Drift chamber tracks are matched to the PC3, by finding the track's expected position in PC3 using the projection of the track's trajectory from the drift chamber to the radius of PC3. The track is rejected if no hits are found in PC3 within a 2 sigma window. The standard deviation of PC3 hits from the track projection is found by measuring the distribution of PC3 hits around track projections. This is done for tracks which pass all other analysis cuts in all other PHENIX detectors and are thus expected to have a high probability of being real charged hadrons. The mean and sigma of these distributions are then found, as shown in figure 3-1 and provided in table 3.2. The p_T and centrality dependence of the mean and sigma of the PC3 matching cuts are shown in figure 3-2. Here, it is observed that the matching cuts are relatively stable with p_T and centrality.

PC3:
$\mu - 2\sigma <$ pc3dphi $< \mu + 2\sigma$ $\mu - 2\sigma <$ pc3dz $\quad < \mu + 2\sigma$
$-2.558 <$ pc3dphi (cm) < 2.245 $-2.495 <$ pc3dz $\quad$ (cm) < 2.187

Table 3.2: Pad chamber 3 (PC3) matching cuts.

3.5.4 Electromagnetic Calorimeter

Since the electromagnetic calorimeter (EMC or EmCal) has a much shorter nuclear interaction length than radiation length, there is a much smaller probability for a hadron to deposit the entirety of its energy in to the EmCal than for an electron or photon. Hadrons, however

EMC dphi for SVXCNT with DCA && SVX && PC3 && DC cits

Counts

h_DCA_SVX_PC3_DC_emcdphi	
Entries	4.890598e+08
Mean	-0.0007247
RMS	0.009553
χ^2 / ndf	9.614e+05 / 18
Constant	-5.164e+05 ± 2.124e+03
Amplitude	4.227e+07 ± 2.661e+03
Mean	-0.0007657 ± 0.0000003
Sigma	0.006819 ± 0.000001

emcdphi (rad)

EMC dz for SVXCNT with DCA && SVX && EMC && DC cits

Counts

h_DCA_SVX_PC3_DC_emcdz	
Entries	4.890598e+08
Mean	1.364
RMS	4.66
χ^2 / ndf	1.322e+05 / 26
Constant	5.558e+05 ± 1.607e+03
Amplitude	2.972e+07 ± 1.991e+03
Mean	1.452 ± 0.000
Sigma	3.014 ± 0.000

emcdz (cm)

PC3 dphi for SVXCNT with DCA && SVX && EMC && DC cits

Counts

h_DCA_SVX_EMC_DC_pc3dphi	
Entries	7.320335e+08
Mean	-0.1584
RMS	2.317
χ^2 / ndf	2.861e+06 / 7
Constant	1.651e+06 ± 6.976e+03
Amplitude	7.287e+07 ± 6.610e+03
Mean	-0.1618 ± 0.0001
Sigma	1.217 ± 0.000

pc3dphi (cm)

PC3 dz for SVXCNT with DCA && SVX && EMC && DC cits

Counts

h_DCA_SVX_EMC_DC_pc3dz	
Entries	7.320335e+08
Mean	1.494
RMS	2.422
χ^2 / ndf	4.276e+04 / 7
Constant	7.216e+06 ± 4.078e+03
Amplitude	7.214e+07 ± 5.518e+03
Mean	1.461 ± 0.000
Sigma	1.045 ± 0.000

pc3dz (cm)

Figure 3-1: The distribution of emcdphi, emcdz, pc3dphi and pc3dz, after all other cuts and fitted to a Gaussian plus constant.
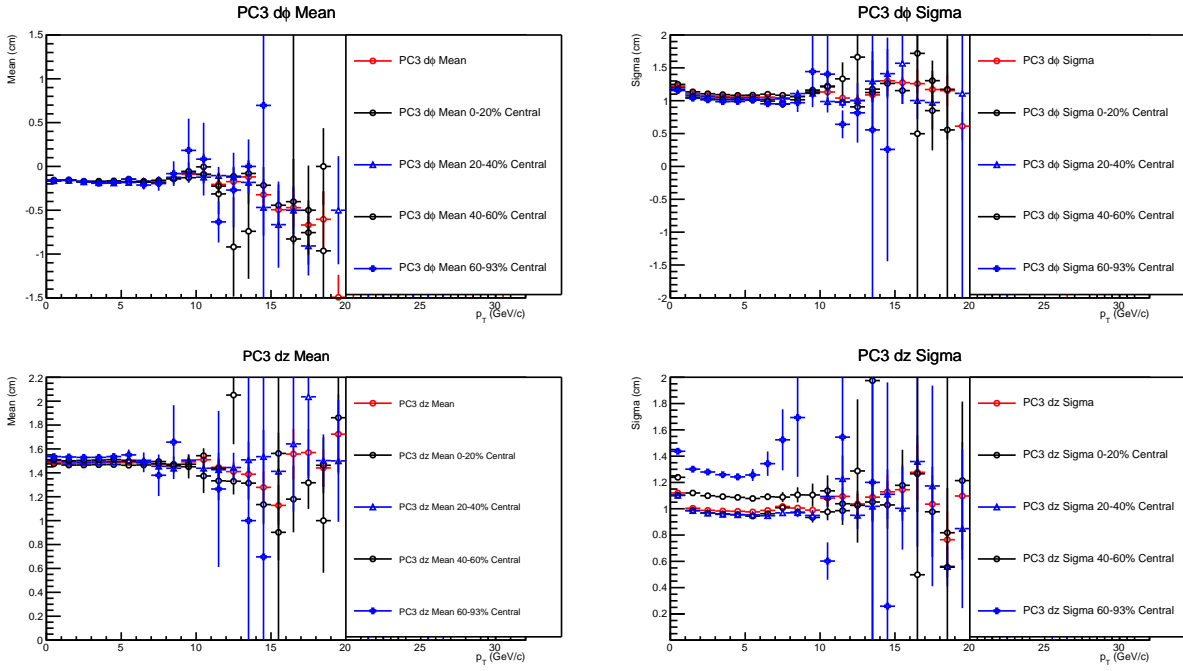
Figure 3-2: Mean and sigma of the PC3 matching variables versus p_T and centrality.
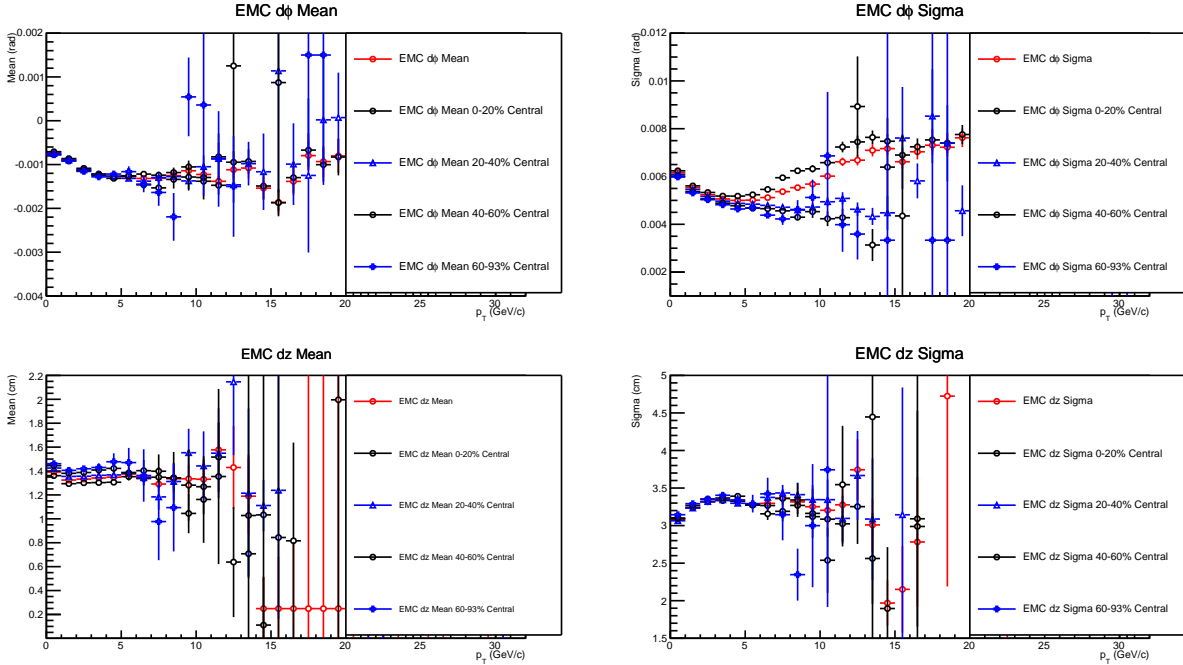
Figure 3-3: Mean and sigma of the EMC matching variables versus p_T and centrality.

29

will still leave hits in the EmCal with a well defined position. Thus, the EmCal can also be used as a confirmation detector during tracking. As with the PC3, drift chamber tracks are projected on to the EmCal, and the distribution of distances from EmCal hits to the projection are measured. These distributions are shown in figure 3-1, and cut values are provided in table 3.3. Only drift chamber tracks which have EmCal hits within $\pm 2\sigma$ are considered signal tracks. The mean and sigma of the EMC matching cuts are shown in figure 3-3.

EMC:		
$\mu - 2\sigma <$ emcdphi $< \mu + 2\sigma$		
$\mu - 2\sigma <$ emcdz $\quad < \mu + 2\sigma$		
$-0.02 \;\; <$ emcdphi (rad) < 0.02		
$-4.701 <$ emcdz $\quad$ (cm) < 7.629		

Table 3.3: Matching cuts in the electromagnetic calorimeter (EMC).

3.6   VTX Cuts

This analysis studies so called SvxCentralTracks (SVXCNT). These are tracks that have been found in the drift chamber and which are projected back towards the collision vertex on to the VTX detector. They are projected on to each layer of the VTX, and then matched to hits located near the projection. In principle, a track could be formed with hits in any number of VTX layers. However, due to computing constraints only tracks with at least 2 hits are saved. Track quality is controlled by the number of hits in the VTX, and the χ^2 of the hits with respect to the track projection.

3.6.1   4 Hit Requirement

The number of layers in the VTX that should be required has been studied at length and will be discuss below in chapter 5. Increasing the number of hits required, greatly increases the

signal purity, but significantly decreases the total acceptance in the VTX. In this analysis, only tracks with at least 4 hits in the VTX are considered (1 hit in each of the four layers). The increase in signal purity gained from going to 4 hit tracks is so great that it out weighs the cost in acceptance loss. Since VTX layers are comprised of partially overlapping sensor ladders, it is possible to find a track with more than 4 hits, but these occur very rarely.

3.6.2 χ^2/NDF

A χ^2 distribution is be obtained after track fitting to hits in the VTX:

$$\chi^2/\text{NDF} = \frac{1}{2N-1}\Big[\sum_{i=0}^{N-1}\Big(\frac{\Delta\phi_i^2}{\sigma_{\phi,i}^2} + \frac{\Delta z_i^2}{\sigma_{z,i}^2}\Big) + \sum_{i=1}^{N-2}\Big(\frac{\Delta\theta_{xy}^2}{\sigma_{\theta xy,i}^2} + \frac{\Delta\theta_{rz}^2}{\sigma_{\theta rz,i}^2}\Big) + \frac{\Delta\theta_{xy,N-1}^2}{\sigma_{\theta xy,N-1}^2 + \sigma_{\phi_0}^2} + \frac{\Delta\theta_{rz,N-1}^2}{\sigma_{\theta rz,N-1}^2 + \sigma_{\theta_0}^2}\Big]$$

(3.1)

Where $N = 4$, is the number of hits in the VTX. The first summation is the contribution to the χ^2 from the positon resolution of the VTX sensors. ϕ_i and z_i are the distances from each hit to the track projection in the in the local coordinate system on the surface of each sensor. The variances $\sigma_{\phi,i}^2$, $\sigma_{z,i}^2$ are determined by the pixel resolution (pixel size/$\sqrt{12}$). The second summmation is the contribution to the χ^2 from the fit. The fit used is a multicircle fit, which fits a helix to each VTX layer and minimizes the deviation of $\Delta\theta$, the angle between the tangent to the helix at layer i and the tangent to the helix at layer $i-1$. σ_θ is the variance in the angle θ, which is determined by multiple scattering. The variances σ_{ϕ_0} and σ_{θ_0} are the contributions from the drift chamber resolution.[20]

This distribution, after applying all other cuts, is shown in figure 3-4. It is fit to a Gaussian plus an exponential tail. A cut is placed on $\chi^2/\text{NDF} < 2\sigma$, where σ is of the Gaussian component.

chi2/ndf for SVXCNT with DCA && SVX && PC3 && EMC && DC cuts

h_DCA_SVX_PC3_EMC_DC_chi2ndf	
Entries	4.561997e+08
Mean	0.979
RMS	0.9878
χ^2 / ndf	2.789e+06 / 6
p0	1.382e+08 ± 3.194e+04
p1	0.9288 ± 0.0001
p2	4.34e+07 ± 4.21e+04
p3	-0.662 ± 0.000

$$p_0 e^{-0.5x^2/p_1^2} + p_2 e^{p_3 x}$$
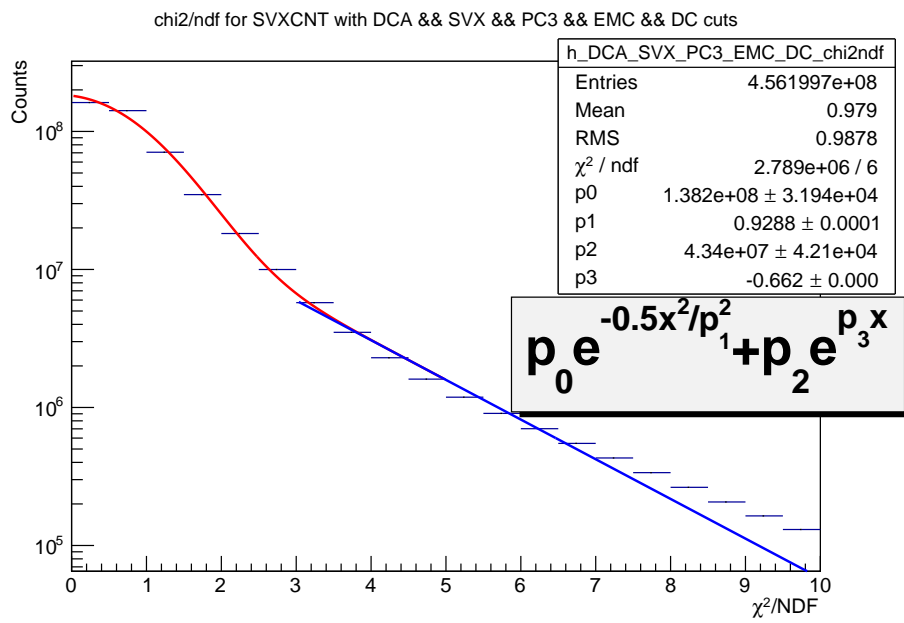
Figure 3-4: χ^2/NDF of SVXCNT tracks after all other cuts and fit to a Gaussian with an exponential tail.

Chapter 4

Distance of Closest Approach Analysis

In addition to VTX track quality cuts, the rejection power of the VTX is further exploited by measuring the distance of closest approach (DCA) of each track. As depicted in figure 4-1, the DCA is defined as the smallest distance between the track projection and the primary collision vertex. The DCA of tracks originating from primary collision products will have a DCA very close to zero. Since the measurements of DCA in the transverse and longitudinal directions are largely independent, the three dimensional DCA vector can be factorized into longitudinal and transverse components. The distribution of DCA centered around zero is smeared by two Gaussian distributions, fluctuations in the beam center location and the inherent resolution of the VTX detector. Together these sources of Gaussian smearing produce a Gaussian shape in the transverse direction with an approximate $\sigma \sim 80$ μm and one in the longitudinal direction with an approximate $\sigma \sim 150$ μm. 2σ DCA cuts are placed in both the transverse and longitudinal directions. Figure 4-3 and figure 4-4 show in blue vertical lines, the cuts placed on DCA_L and DCA_T respectively.
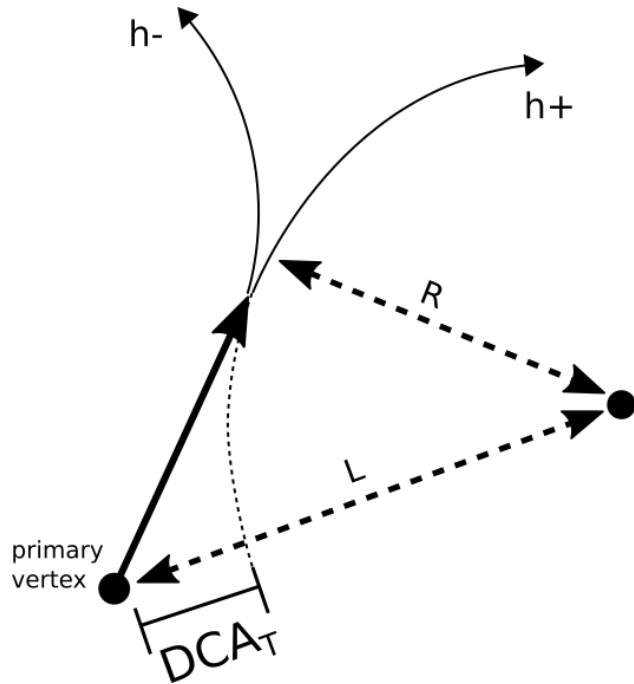
Figure 4-1: Distance of closest approach (DCA) is measured by projecting a track back to the primary collision vertex and measuring the distance between its closest point.

4.0.1 Secondary Decay Products from Weakly Decaying Particles

Below 6.0 GeV/c, an additional contribution to the DCA distribution appears from secondary decay products of weakly decaying particles. These additional background tracks form an exponential tail in the DCA distribution with a width much larger than the Gaussian peak, as can be seen in figure 4-2. The contribution of this weak decay background to the DCA is estimated by fitting the sidebands to exponentials (the fit range is shown within the vertical blue lines on figure 4-2). The exponential is then subtracted leaving the Gaussian plus combinatorial background shown by blue circles. Across the spectrum, the contribution to the DCA distribution from weakly decaying particles is always $< 1\%$ of the contribution from real charged hadrons.
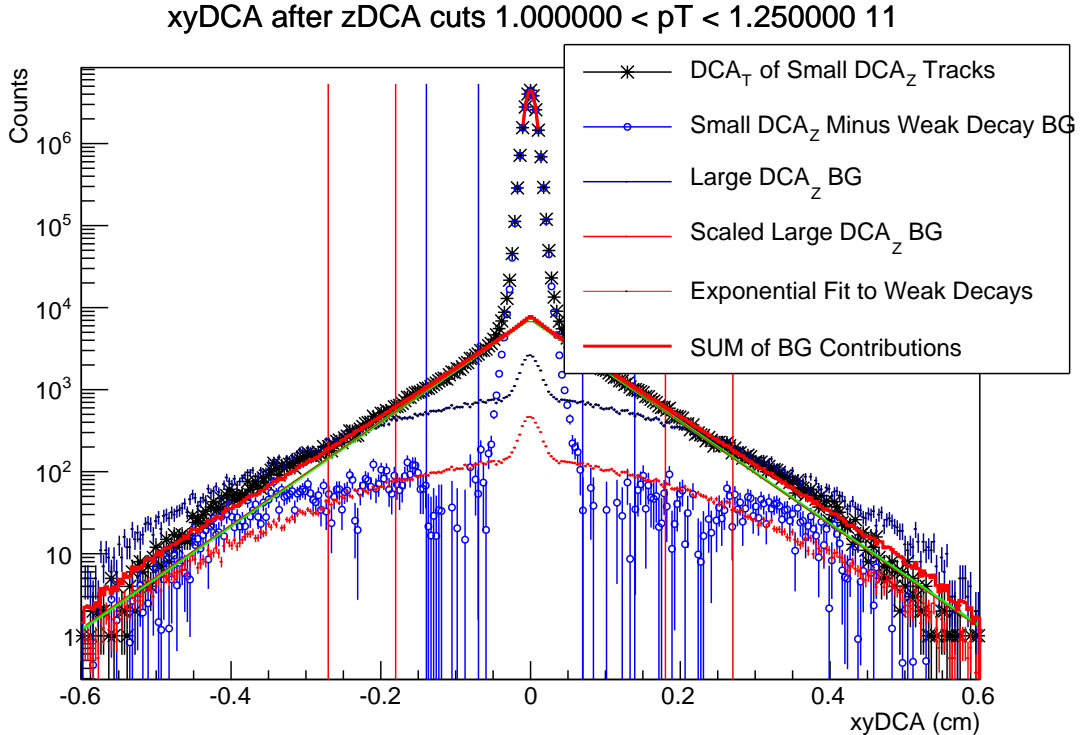
Figure 4-2: DCA in the transverse direction for $1.0 < p_T < 1.25$ GeV/c after cuts on the longitudinal DCA (stars). Sidebands from secondary weak decay products are fit to an exponential (red line) and subtracted (blue circles). The DCA_T of tracks with large DCA_Z (black points) are scaled to the remaining side bands (red points).

4.0.2 DCA Shape

Combinatorial background tracks will have a randomly, although not necessarily flat, DCA distribution. Thus, even after cutting on both transverse and longitudinal DCA, and subtracting contributions from weak decays, there still remains background present under the DCA peak. This combinatorial background will be subtracted, by looking at the shape of the transverse DCA distribution for tracks with very large longitudinal DCA. These tracks are expected to be background tracks. This background shape is then scaled up to the side bands of the transverse distribution and subtracted.

Tracks with Large Longitudinal DCA

Where tracks from real charged hadrons are expected to have a Gaussian three dimensional DCA close to 0, background tracks have a largely randomly distributed three dimensional DCA. Thus, tracks with a large longitudinal DCA are likely background tracks with the same transverse DCA distribution as random background tracks at small longitudinal DCA. The shape of the combinatorial background in the transverse direction, is obtained by plotting the transverse DCA (DCA_T) for tracks with very large longitudinal DCA (DCA_L). To define very large longitudinal DCA, for each p_T bin, DCA in both directions is fit to a Gaussian as shown in figures 4-3 and 4-4 for $1.0 < p_T < 1.25$ GeV/c. Tracks with very large longitudinal DCA are defined as tracks with a $DCA_L > 12\sigma$, shown as the portions of the distribution outside the red vertical lines in figure 4-3.

The DCA_T for tracks with large DCA_L is shown in figure 4-2 as dark blue points. These points are not yet properly normalized and appear larger than the distribution of $DCA_L < 2\sigma$ tracks in some regions. To normalize the background distribution, it is scaled down to the sidebands of the small DCA_L tracks at large DCA_T which is known to be background. The regions defined as sidebands are shown in figure 4-2 between the vertical red lines. Scaling is done using the integrals of each distribution in the side band region. Normalizing results in the distribution shown as red points, which is the normalized shape of large longitudinal DCA background. Below 6.0 GeV/c, where secondary products of weak decays contribute to the DCA, sideband scaling is performed after the exponentially shaped weak decay DCA is subtracted.

4.0.3   Binning

Due to the decreasing amount of statistics at high p_T, it becomes useful to combine p_T bins in order to preserve a clear Gaussian shape of the DCA peak until as high a p_T as possible,
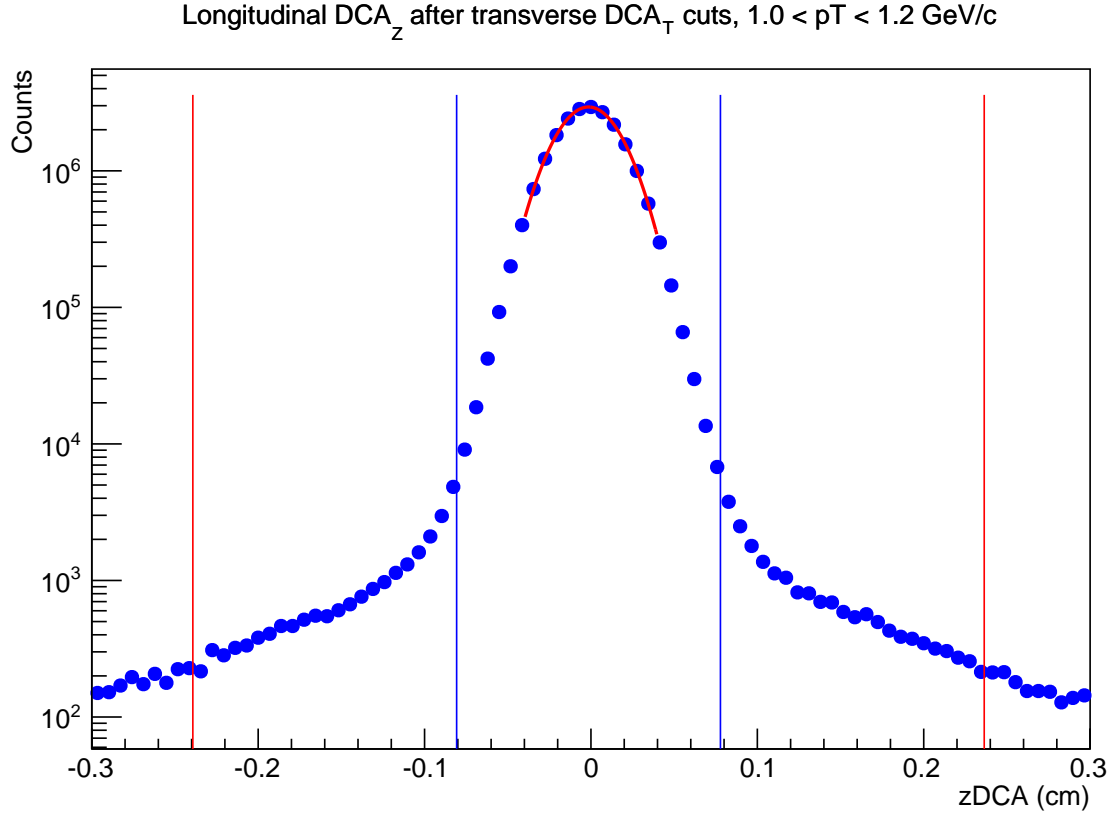
Figure 4-3: DCA in the longitudinal direction for $1.0 < p_T < 1.25$ GeV/c. Points inside of the blue vertical lines pass the 2σ DCA cuts. Points outside of the red vertical lines are considered high DCA_L.

to this end the DCA distributions are binned as a function of p_T according to the schema shown in table 4.1.

4.0.4 Mean and Sigma Extrapolation

Above $p_T > 12$ GeV/c, the decrease in the amount of statistics limits the accuracy of the measurements of the mean and sigma of both DCA_T and DCA_L. These quantities determine the size of the DCA cuts, as well as the definitions of large and small DCA for the statistical subtraction of the random combinatorial background as discussed above. Therefore, an accurate parameterization of them at high p_T is crucial. To this end the μ
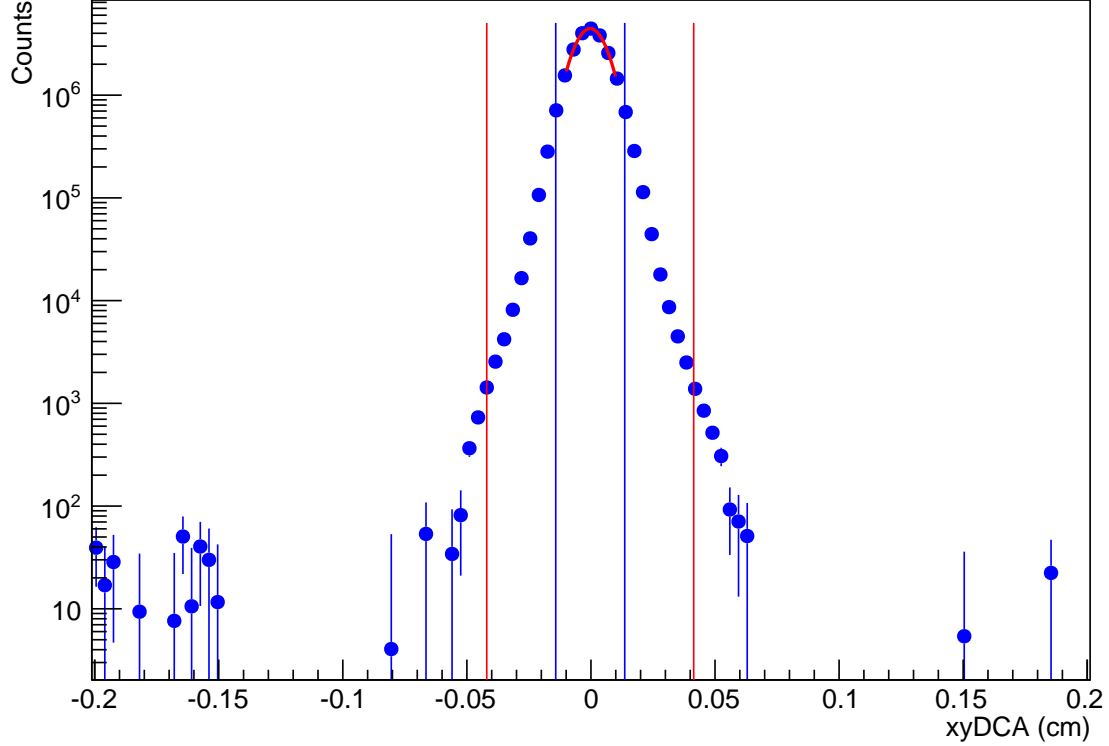
Figure 4-4: DCA in the transverse direction for $1.0 < p_T < 1.25$ GeV/c after background subtraction. Points inside of the blue vertical lines pass the 2σ DCA cuts. Points outside of the red vertical lines are consider high DCA_T.

and σ of DCA_T and DCA_L are extrapolated from low to high p_T. Figure 4-5 shows how the mean (filled squares) and sigma (hollow squares) for both longitudinal (red) and transverse (blue) DCA. $\sigma(\mathrm{DCA}_T)$ initially decreases exponentially and then flattens out after 4 GeV/c. Accordingly, $\sigma(\mathrm{DCA}_T)$ is fit to a decaying exponential plus a constant $\sigma_{\mathrm{DCA}_T}^{\mathrm{High}p_T}$. Above 12 GeV/c, $\sigma = \sigma_{\mathrm{DCA}_T}^{\mathrm{High}p_T}$ is used to determine the cuts on DCA_T. Similarly, in the longitudinal direction, $\sigma(\mathrm{DCA}_L)$ decays exponentially at low p_T, then increases linearly until 7 GeV/c where it flattens out. Subsequently, $\sigma(\mathrm{DCA}_L)$ is fit to the constant $\sigma = \sigma_{\mathrm{DCA}_L}^{\mathrm{High}p_T}$ above 7 GeV/c. Above 12 GeV/c $\sigma = \sigma_{\mathrm{DCA}_L}^{\mathrm{High}p_T}$ is used to define the cuts on DCA_L as well as the definitions of large and small DCA_L.
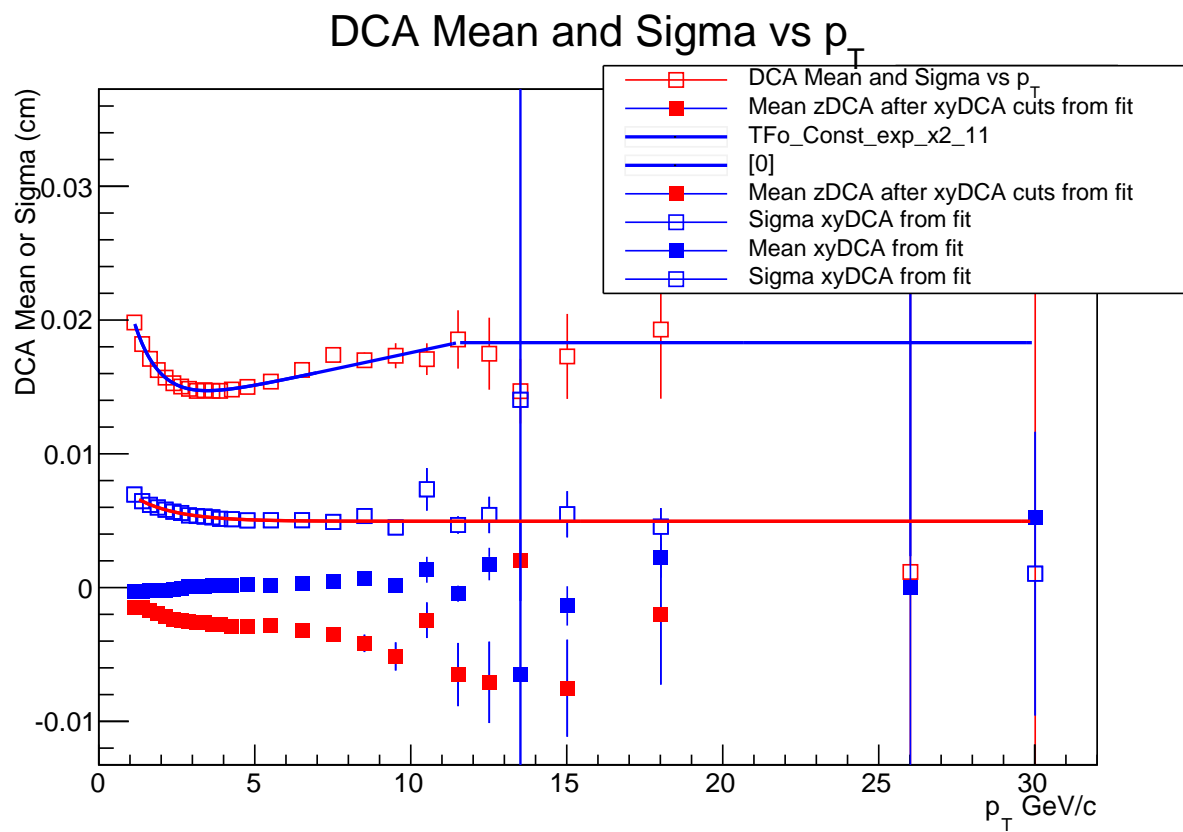
Figure 4-5: Transverse and longitudinal DCA mean and sigma versus p_T.

p_T Range	Bin Size
$1 \le p_T < 5$	0.5 GeV/c
$5 \le p_T < 14$	1.0 GeV/c
$14 \le p_T < 16$	2.0 GeV/c
$16 \le p_T < 24$	4.0 GeV/c

Table 4.1: DCA distribution p_T bin widths as a function of p_T. p_T bin width increases with p_T in order to resolve a Gaussian DCA structure to as high a p_T as possible.

4.0.5 DCA Distributions at high p_T

As shown in figure 4-6, the transverse DCA exhibits a clear Gaussian shape up to ~ 18 GeV/c. Above 18 GeV/c, due to the limited statistics, the distribution's shape can no longer be discerned. It is believed, however, that the points above 18 GeV/c are real charged hadrons. Calculating the remaining background after all VTX cuts shows that the signal to background ratio remains well above one up to $\gtrsim 46$ GeV/c. This calculation is shown in full detail in the next section.
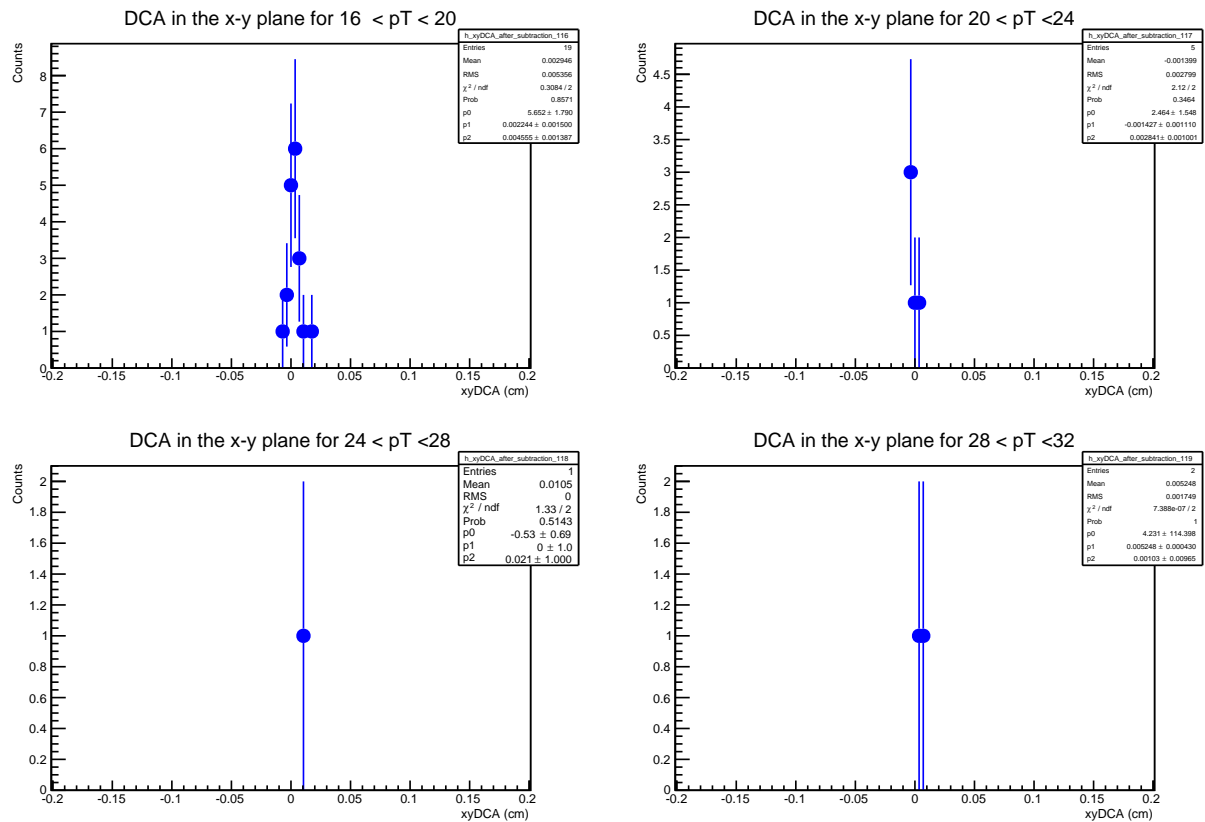
Figure 4-6: Transverse DCA at very high p_T.

Chapter 5

Background Rate Estimate

5.1 Introduction

The main constraint on measuring the charged hadron spectrum is the background from sources which do not originate from the primary vertex, and are misreconstructed by the drift chamber as high-p_T charged hadrons. Background tracks from off-vertex sources are significantly reduced by matching central arm tracks to hits in the VTX. As discussed above, the VTX consists of 4 concentric barrels of silicon sensors, positioned close (between 2.53 cm and 16.69 cm) to the beam center. Tracks reconstructed in the drift chamber are projected back into the barrels of the VTX and associated with sensor hits forming a new track object called an SVX central track (SVXCNT). In this analysis, SVXCNT tracks are required to have 4 associated hits in the VTX. Tracks are also rejected statistically based on distribution of the distance of closest approach (DCA) as discussed in previous sections. After the DCA analysis, there remains some background under the DCA peak. This remaining background can be explained by random combinations of central arm tracks and either correlated or uncorrelated hits in the 4 layers of the VTX. Correlated hits originate from a single charged hadron track passing through the VTX and uncorrelated hits come from a random alignment

of hits from 4 independent VTX tracks.

In the following sections, a method for estimating a priori the rate of fake SVXCNT tracks formed by matching central arm tracks to hits in the VTX is shown for two cases. First, the rate of tracks formed by association of random and uncorrelated hits in the 4 layers of the VTX with an off-vertex track in the central arm is considered. Second, the rate of fake tracks formed by the random combination of an off-vertex track in the central arm with 4 correlated hits created by a real charged hadron passing through the VTX is calculated. Finally, both calculated rates are compared to the background measured by examining the DCA shape. Here, its is observed that much of the remaining background is caused by the fake SVXCNT tracks formed from correlated hits in the VTX.

One remaining source of background which has not been considered is the possibility of a mix of uncorrelated and correlated VTX hits. For example, a real charged hadron may produce a 3 hit VTX standalone track which is associated with a random hit in the fourth layer when forming a SVXCNT track. This would create an additional source of background which has not been taken into account here. However, since 4 hit tracks are requred, mathching a 2 or 3 hit correlated track to additional random uncorrelated hits is very unlikely.

5.2 Uncorrelated Background from Random Association of Hits

Candidate charged hadron tracks are formed by projecting drift chamber tracks on to the outermost layers of the VTX. When 4 hit tracks are required, the outer most layer is always barrel 3 (B3). If a hit is found within the search window of the outer most layer, the track is confirmed by looking for hits in the search windows of subsequent layers. The size of

B0	$\frac{0.05\text{mm}\times0.425\text{mm}}{2.63\text{mm}\times2.63\text{mm}}$	= 3.07E-3
B1	$\frac{0.05\text{mm}\times0.425\text{mm}}{5.13\text{mm}\times5.13\text{mm}}$	= 8.07E-4
B2	$\frac{0.08\text{mm}\times1\text{mm}}{11.77\text{mm}\times11.77\text{mm}}$	= 5.77E-4
B3	$\frac{0.08\text{mm}\times1\text{mm}}{16.69\text{mm}\times16.69\text{mm}}$	= 2.87E-4

Table 5.1: Pixel occupancy for each VTX layer.

these search windows are determined from multiple scattering and other factors discussed below. The rate per event of fake SVXCNT tracks formed from the random combination of central arm off-vertex tracks and 4 uncorrelated random hits in the VTX can be calculated by multiplying the number of off-vertex tracks in the central arm (N_{seed}) times the product of the probabilities of finding a random hit in each layer of the VTX (P_i). These probabilities can be calculated from the occupancy within the search window in each layer.

$$P(\text{Uncorrelated}) = N_{seed} \times \prod_{i=1}^{4} P_i \tag{5.1}$$

5.3 Pixel Occupancy in Each Layer of the VTX

5.3.1 Seed Tracks

First, the occupancy of each pixel is calculated. The innermost barrels of the VTX (B0 and B1) are pixel detectors, made up of small pixel like silicon sensors. The outermost layers (B2 and B3) are comprised of elongated strippixels, but for the fake rate analysis we will refer to both the pixel sensors and strippixel sensors as pixels, because we are interested in the occupancy of the smallest units of each detector. This occupancy can be estimated from the average event multiplicity[10]. For central collisions:

$$\frac{dN}{d\eta} \sim 600 \tag{5.2}$$

44

$$\frac{dN}{d\eta} \sim \frac{dN}{d\theta} = \sin(\theta)2\pi\frac{dN}{d\Omega} \sim 2\pi\frac{dN}{d\Omega} \rightarrow \frac{dN}{d\Omega} \sim 100 \text{ tracks} \tag{5.3}$$

Thus the area within which on average 1 track is found (as a function of radius)[10]:

$$\int_0^{1track} dN = 100 \iint_{1track} d\Omega = 100 \iint_{Area} \frac{\hat{r} \cdot \hat{n} ds}{r^2} = 100\frac{A}{r^2} \tag{5.4}$$

$$A = \frac{r^2}{100} = \frac{r}{10} \times \frac{r}{10} \tag{5.5}$$

The pixel occupancy is the area of one pixel divided by the average area to find 1 track, as shown in table 5.1.

To find the spectrum of off-vertex central arm tracks N_{seed}, first we consider the signal spectrum of charged hadron tracks, found after performing the full VTX charged hadron measurement. This is the uncorrected spectrum after the complete analysis, which will be discussed in greater detail in chapter 6. The spectrum of charged hadron tracks, uncorrected for efficiency, as found after the VTX analysis is shown in figure 5-1. This spectrum is taken to be the signal spectrum and is fit to a Hagedorn function at low p_T with a Woods-Saxon transition to a power law at high p_T:

$$S(p_T) = W(p_T)p_2[1 + p_T/p_3]^{-p_4} + [1 - W(p_T)]p_5 p_T^{-p_6}, W(p_T) = [1 + e^{\frac{p_T - p_0}{p_1}}]^{-1} \tag{5.6}$$

The parameters of the fit are shown in table 5.2.

The spectrum of central arm tracks is separated into signal and background components, assuming that the signal shape is $S(p_T)$. The total sample of central arm tracks is taken to be drift chamber tracks matched geometrically to both the EMC and PC3. The tracks pass the same set of DC, EMC and PC cuts as the SVXCNT tracks used in the main analysis.

This sample of tracks is shown as the blue square data points in figure 5-2. In order to estimate the number of off-vertex background tracks present in the central arms, they are fit to a function $T(p_T)$. Where $T(p_T)$ is the signal function $S(p_T)$ determined above, multiplied by an efficiency factor p_7, plus a model of the background shape $B(p_T)$:

$$T(p_T) = p_7 S(p_T) + B(p_T) \tag{5.7}$$

for

$$B(p_T) = p_8 + p_9(p_T)^{p_{10}} \tag{5.8}$$

After fitting, the function $T(p_T)$ is shown in figure 5-2 as the red curve, the signal component $S(p_T)$ is shown as the black curve and the background component $B(p_T)$ as the blue curve. Figure 5-3 shows the ratios of $S(p_T)$ and $B(p_T)$ to $T(p_T)$ and table 5.3 shows the additional parameters to the fit. The number of background seed tracks for the fake rate estimate is then calculated per p_T by integrating $B(p_T)$ over each p_T bin.

p_0 (GeV/c)	4.99976	p_4	1.16351e+07
p_1 (GeV/c)	-1.06712e+12	p_5 (mbarn GeV^{-2}/c^3)	2.12811e+10
p_2 (mbarn GeV^{-2}/c^3)	-6.3471e+11	p_6	7.71079
p_3 (GeV/c)	2.54442e+06		

Table 5.2: Parameters of the fit of the uncorrected yield of charged hadrons in Run-11 after normalizing by the number of events.

p_7	0.635284	p_8	7.77156e-11
p_9	1.01566e+08	p_{10}	2.3

Table 5.3: Parameters of the fit of the spectrum of matched central arm tracks.
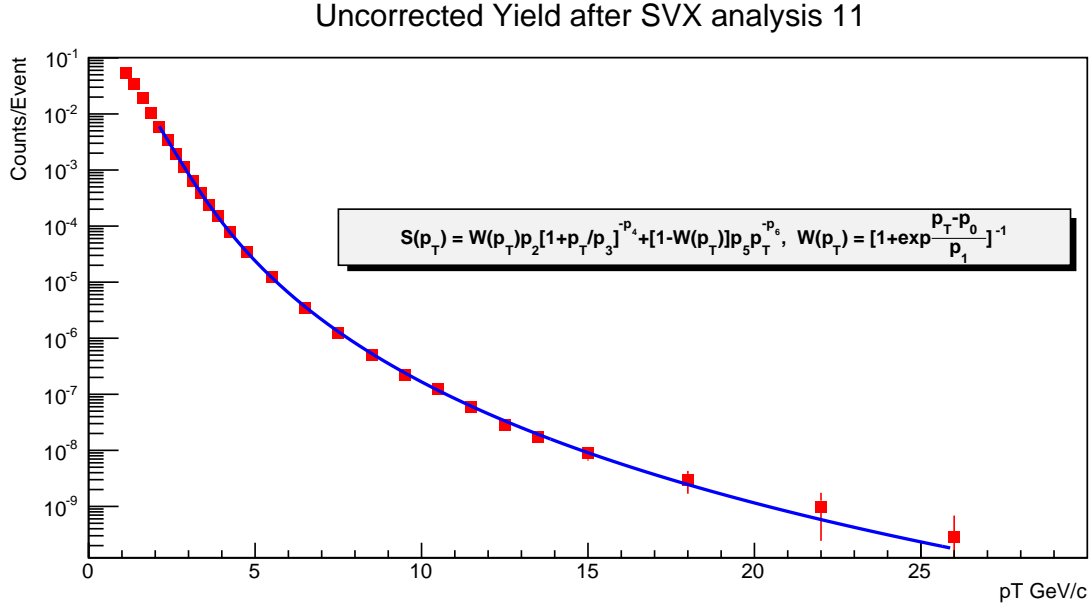
Figure 5-1: Spectrum of charged hadrons after Run-11 VTX charged hadron analysis. Fit to a Hagedorn function at low p_T with a Woods-Saxon transition to a power law at high p_T.

5.3.2   Outer Layer Confirmation Probability

The probability of confirming a central arm track with a hit in the outer layer of the VTX is given in equation 5.9:

$$\frac{\text{(Area of the search window)}}{\text{(Average Area to find 1 track)}} = (\#\text{of pixels in the search window}) \times (\text{pixel occupancy})$$

(5.9)

The size of the search window on the outer layer depends on the angular resolution of the drift chamber, the intrinsic resolution of the beam center and multiple scattering.

The Azimuthal Component of the Search Window

The search windows on the VTX layers can be split into lengths along the azimuthal and longitudinal direction. The azimuthal direction will be considered first.

47
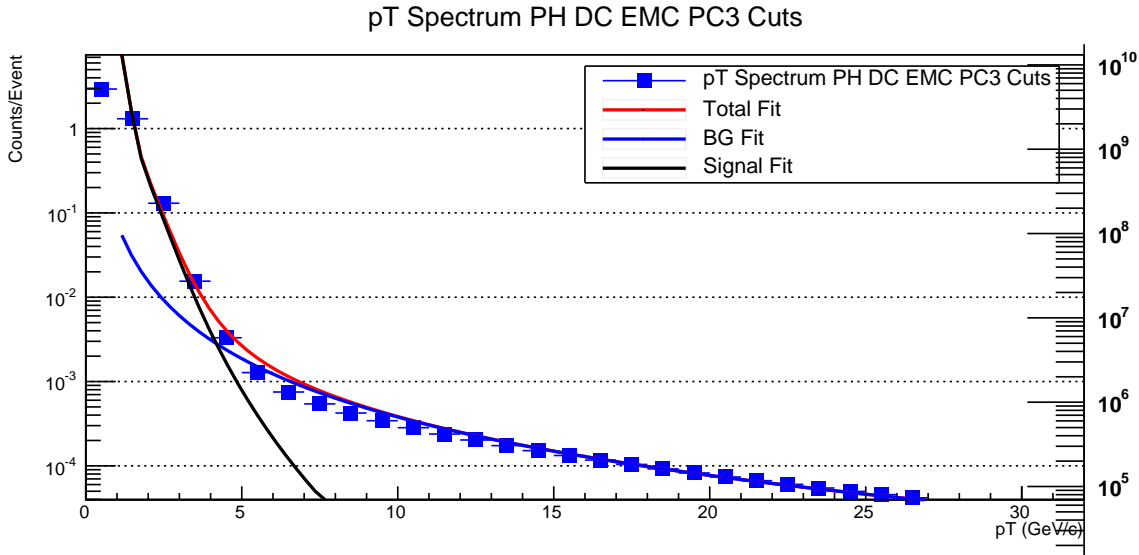
Figure 5-2: Spectrum of drift chamber tracks matched to the EMC and PC3. Fit of the background is shown in blue, signal in black and total in red.
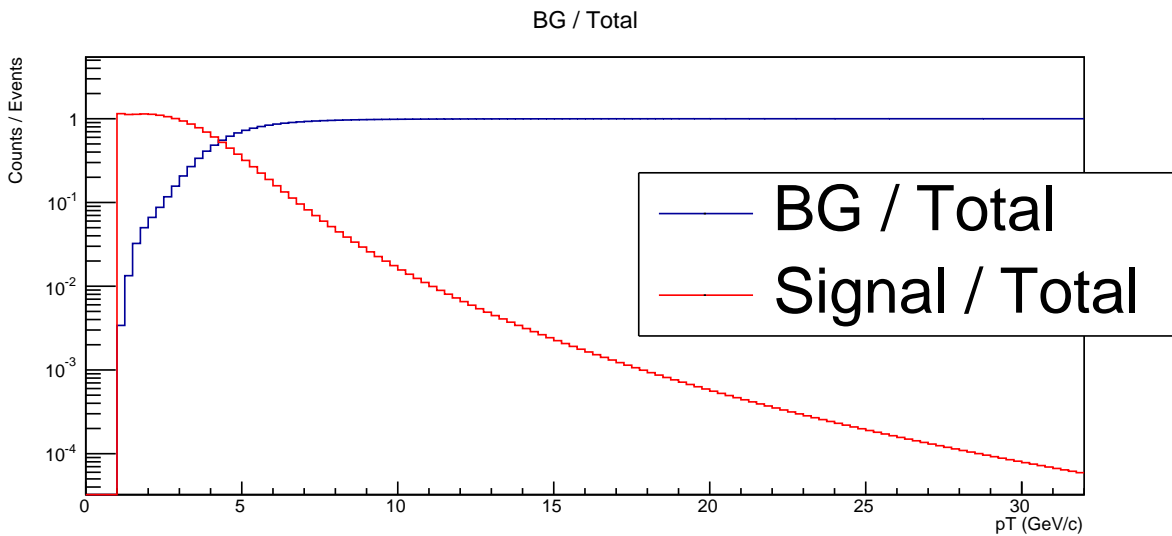
Figure 5-3: Red: Ratio of the extracted signal to the total central arm track spectrum $(S(p_T)/T(p_T))$. Blue: Ratio of the extracted background over the total central arm track spectrum ($B(p_T)/T(p_T)$). As expected, the signal dominates at low p_T and the background dominates at high p_T.
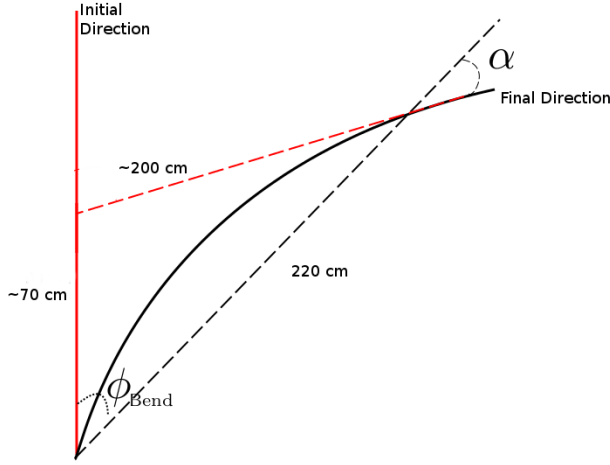
Figure 5-4: Drift chamber angular resolution projected onto VTX.

x/x_0 Air B3-DC	0.67%
x/x_0 B0	1.28%
x/x_0 B1	1.28%
x/x_0 B2	5.66%
x/x_0 B3	4.51%

Table 5.4: Radiation lengths of the different VTX barrels (B0-B3), as well as the air in between the VTX and the drift chamber (B3-DC).

Effect of Angular Resolution on Outer Layer Confirmation Probability

The PHENIX drift chamber has an angular resolution of $\Delta\alpha = 1$ mrad[9]. This corresponds to a 2.857 mrad uncertainty in the bending angle Φ seen by the outer layer of the VTX (see fig. 5-4):

$$\sin(\Phi) \sim \frac{200}{70}\sin(\alpha) = 2.857\alpha \rightarrow \Delta\Phi \sim 2.857 \text{ mrad} \qquad (5.10)$$

Effect of Multiple Scattering on Outer Layer Confirmation Probability

Multiple scattering introduces an additional uncertainty on the projection of the central arm track on to the outer layer of the VTX. The projection is affected by both the multiple

p_T (GeV/c)	1.0	5.0	10.0	15.0	20.0
θ_0 (mrad) B0	1.284	0.257	0.128	0.086	0.064
θ_0 (mrad) B1	1.284	0.257	0.128	0.086	0.064
θ_0 (mrad) B2	2.882	0.576	0.288	0.192	0.144
θ_0 (mrad) B3	2.548	0.510	0.255	0.170	0.127
θ_0 (mrad) B0-B3	4.254	0.851	0.425	0.284	0.213

Table 5.5: The multiple scattering angle θ_0 for each layer of the VTX for 5 example p_T bins.

scattering between layers of the VTX and the multiple scattering through the air between the VTX and the drift chamber. To find the total multiple scattering angle in the VTX, the multiple scattering angles in each layer are added in quadrature. Table 5.4 shows the radiation lengths of the different VTX barrels (B0-B3), as well as the radiation length of the air in between the VTX and the drift chamber (B3-DC). The deviation in angle (θ_0) from multiple scattering after passing through a thin piece of material such as a VTX layer is [25]:

$$\theta_0 = \frac{12.6 \text{ MeV}}{\beta c p} z \sqrt{\frac{x}{X_0}} [1 + 0.038 \log \frac{x}{X_0}] \tag{5.11}$$

which results in the multiple scatterings in the VTX shown in table 5.5 for 5 example p_T bins.

The angular deviation $\Delta\theta$ after exiting a continuous region of material is approximately $\theta_0/\sqrt{3}$ (See figure 5-5), where θ_0 is given by equation 5.11[25]. This results in an uncertainty in the angle on B3 of $\Delta\Phi_{\text{air}} \sim 2.857\Delta\theta$ as seen by the VTX (see preceding subsection). Table 5.6 provides the angular deviation from multiple scattering in air, $\Delta\Phi_{\text{air}}$, as well as the final angular deviation from multiple scattering $\Delta\Phi_{\text{tot}} = \sqrt{\Delta\Phi_{\text{air}}^2 + \theta_{0,B0-B3}^2}$.

p_T (GeV/c)	1.0	5.0	10.0	15.0	20.0
$\Delta\Phi_{\text{air}}$ (mrad)	1.4830	0.297	0.148	0.099	0.074
$\Delta\Phi_{\text{tot}}$ (mrad)	5.335	2.996	2.892	2.873	2.866

Table 5.6: The multiple scattering angular deviation at B3 from the air between the VTX and the drift chamber, as well as the final angular deviation, computed by adding the components in quadrature.
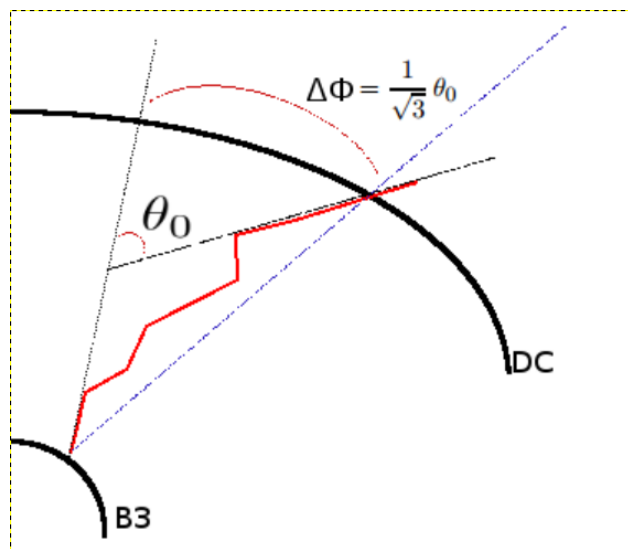
Figure 5-5: Effect of multiple scattering due to the air between the Drift chamber and the VTX.

p_T (GeV/c)	1.0	5.0	10.0	15.0	20.0
$\Delta\Phi_{\text{tot}}$ (mm)	3.567	2.010	1.941	1.928	1.914

Table 5.7: The search window width in the azimuthal direction.

Effect of Vertex Resolution on Outer Layer Confirmation Probability

The above calculation of Φ assumed the track originated exactly from the primary vertex, however the nonzero vertex resolution must be taken into account. This is done by adding the DCA resolution in quadrature with the arc length carved out by the angular uncertainties calculated above.

Final Azimuthal Component of Search Window

The uncertainty in Φ accumulated thus far from the drift chamber resolution and multiple scattering can be translated into the azimuthal width of the search window by multiplying by the radius of B3: $dS_{\text{B3}} = r\Delta\phi$. This azimuthal width is then added in quadrature with the DCA resolution to take into account the beam center resolution. Finally, this width is multiplied by a factor of 4.0 to model a window spanning $\pm 2\ \sigma$, as the VTX tracking algorithm uses $\pm 2\ \sigma$ windows. The final width of the search window in the ϕ direction is given in table 5.7.

The Longitudinal Component of the Search Window

The longitudinal width of the search window is determined by the longitudinal resolution of the drift chamber, the beam center resolution and multiple scattering. The drift chamber has a longitudinal resolution of ~ 2 mm which corresponds to an angular resolution of ~ 0.9 mrad (see figure 5-6):

$$2\tan(1\ \text{mm}/2200\ \text{mm}) = 2\ \text{mm}/2200\ \text{mm} = 0.909\ \text{mrad} \tag{5.12}$$
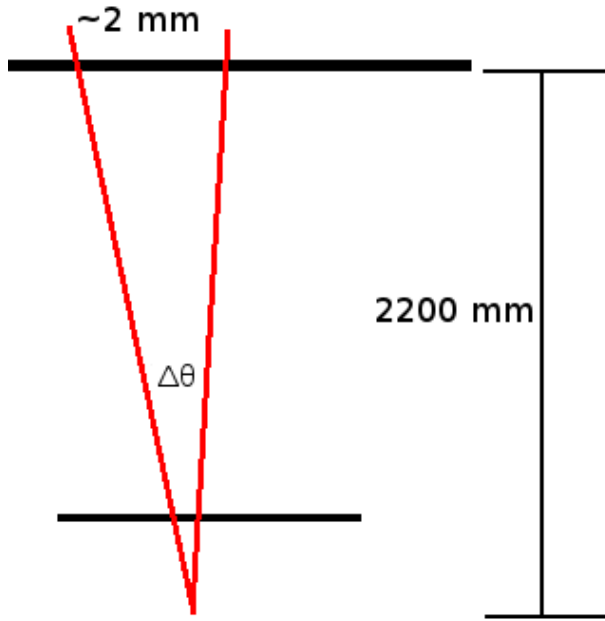
Figure 5-6: In the longitudinal direction, the angular resolution of the drift chamber is twice the tangent of half the linear resolution divided by the radius which is approximately the linear resolution divided by the radius.

p_T (GeV/c)	1.0	5.0	10.0	15.0	20.0
ΔZ_{tot} (mm)	2.978	1.005	0.874	0.848	0.838

Table 5.8: The search window width in the longitudinal direction.

Multiple scattering creates an angular deviation of the same magnitude in the longitudinal direction as in the azimuthal direction. Thus, the deviation from multiple scattering is the same as for the azimuthal direction as is shown in the last line of table 5.6. Adding the DC resolution, multiple scattering and vertex resolution in quadrature and multiplying by 4 for $\pm 2\,\sigma$ window, yields the final longitudinal widths of the search window shown in table 5.8.

Final Outer Layer Confirmation Probability

The number of pixels covered by the search area can be calculated by dividing azimuthal and longitudinal search window widths by the azimuthal and longitudinal pixel widths re-

p_T (GeV/c)	1.0	5.0	10.0	15.0	20.0
ϕ length in # of pixels	45	26	25	25	25
Z length in # of pixels	3	2	2	2	2
Window Area in # of pixels	135	52	50	50	50
Probability B3	3.875%	1.492%	1.435%	1.435%	1.435%

Table 5.9: Outer layer search window in units of pixels as well as the final outer layer probability for 5 example p_T bins.

spectively. Multiplying the azimuthal and longitudinal widths together produces the search window area in units of pixels. Multiplying by the pixel occupancies then yields the probability of finding a random hit in B3, the outer layer of the VTX. The search window widths and area in units of pixels as well as the final probabilities are given in table 5.9. Widths are constrained to be greater or equal to 2 pixels, since the clustering algorithm requires at least 2 pixels to form a cluster.

5.3.3   Inner Layer Confirmation Probabilities

The Azimuthal Component of the Search Window

The search windows for matching hits in inner layers are predominately determined by multiple scattering. The search window in an inner layer is set by the multiple scattering in the layer above, i.e. the uncertainty in layer B2 is due to the multiple scattering in B3 (see figure 5-7). This is due to the fact, that particles travel through the barrels in ascending order, but the track projection from the drift chamber tracks back through the VTX layers in descending order. For example, as a particle multiple scatters in B3, this changes the sweep of the angle needed to look for hits in B2. Table 5.10 shows the uncertainty on the inner layers due to multiple scattering.
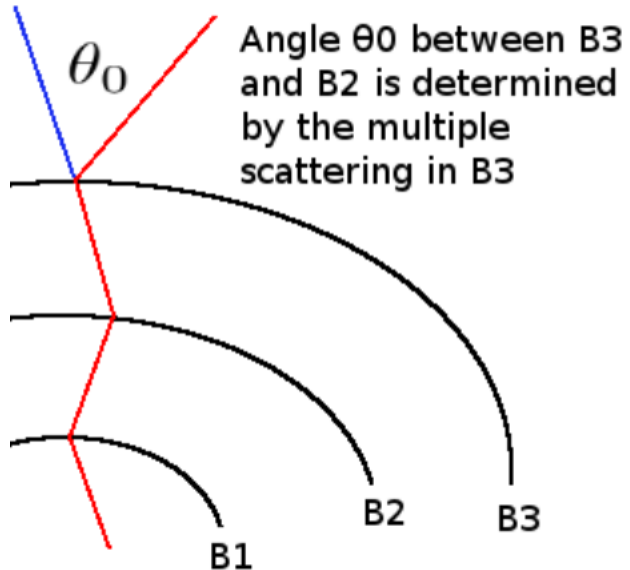
Figure 5-7: The search window in an inner layer is set by the multiple scattering in the layer above, i.e. the uncertainty in layer B2 is due to the multiple scattering in B3.

p_T (GeV/c)	1.0	5.0	10.0	15.0	20.0
θ_0 B2 to B3 (mrad)	2.548	0.510	0.255	0.170	0.127
θ_0 B1 to B2 (mrad)	2.882	0.576	0.288	0.192	0.144
θ_0 B0 to B1 (mrad)	1.284	0.257	0.128	0.086	0.064

Table 5.10: Uncertainty in the inner layers due to multiple scattering.

p_T (GeV/c)	1.0	5.0	10.0	15.0	20.0
B2 Window in # of pixels	16	4	4	4	4
B1 Window in # of pixels	32	8	4	4	4
B0 Window in # of pixels	6	4	4	4	4
B2 Probability for a Random Hit	0.92%	0.23%	0.23%	0.23%	0.23%
B1 Probability for a Random Hit	2.58%	0.65%	0.32%	0.32%	0.32%
B0 Probability for a Random Hit	1.84%	1.23%	1.23%	1.23%	1.23%

Table 5.11: The search windows and random hit probabilities in the inner layers.

The Longitudinal Component of the Search Window

In the longitudinal direction, the uncertainty from multiple scattering is always smaller than width of two pixels. Since two pixels is the minimum number required to form a cluster, the longitudinal width of the search window is always taken to be 2 pixels in each of the inner layers.

Final Probabilities for Inner Layer Confirmation Hits

The inner layer search windows for $\pm 2\ \sigma$ and the resulting probabilities are shown in table 5.11.

5.3.4 Fake Rate Spectrum for Uncorrelated Hits

The spectrum of background tracks formed from an off-vertex drift chamber track matched to 4 random and uncorrelated hits in the VTX is obtained by finding the product of N_{seed} with the probability of finding a random hit on each layer. The resulting spectrum is plotted as black stars on figure 5-8. Also plotted on figure 5-8 is the uncorrected charged hadron signal spectrum in red squares and the measured background level under the DCA peak in black circles. The fake rate of uncorrelated SVXCNT tracks appears to be about two orders

Uncorrected Run 11 AuAu Charged Hadron Spectrum
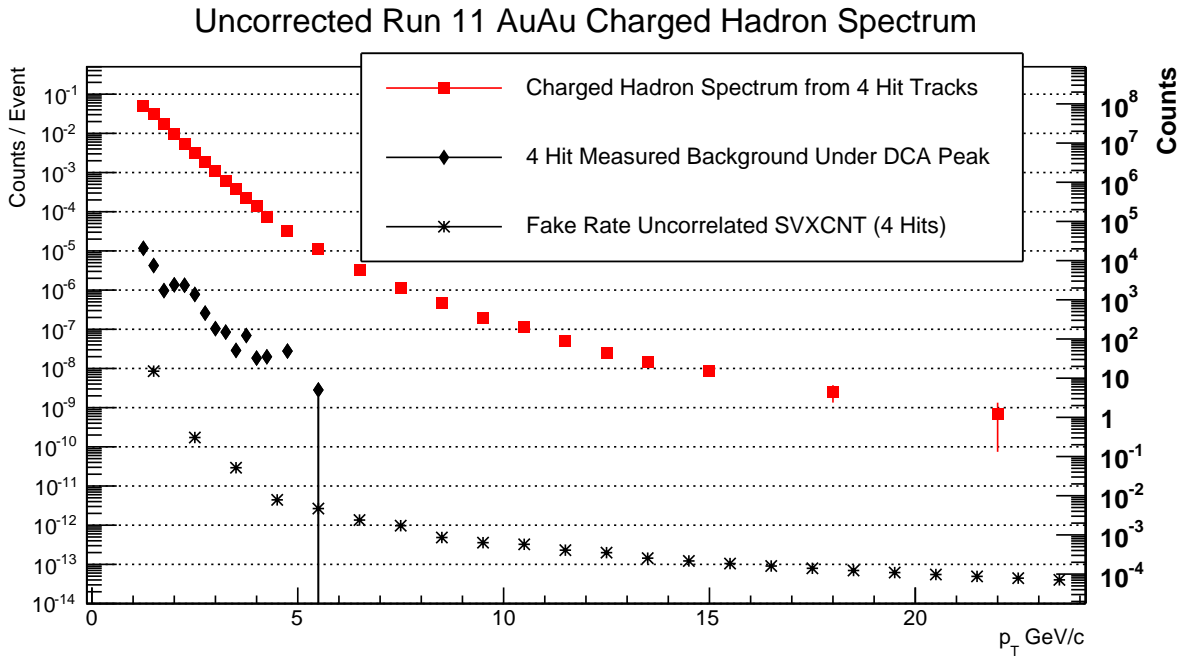
Figure 5-8: Uncorrected charged hadron spectrum (Red). Background remaining under the DCA peak (Black Diamonds). Estimate of uncorrelated fake SVXCNT tracks (Black Stars).

of magnitude under the measured background. As will be seen in the next section the fake rate of SVXCNT tracks from randomly associated tracks contribute, more significantly to the background.

5.4 Correlated Background from Random Association of Tracks

In the previous section, the rate of fake SVXCNT tracks formed by off-vertex central tracks projected onto random and uncorrelated hits in each layer of the VTX was calculated. Another possible source of fake SVXCNT tracks is the random combination of an off-vertex central arm track with a real charged hadron in the VTX. In other words, an off-vertex central arm track matched with a set of correlated hits in the VTX. The spectrum of these background tracks can be estimated by multiplying the number of off-vertex central arm tracks times the number of true charged hadron tracks that randomly have the same spatial positions and angular trajectories. The spectrum of these tracks is given by:

$$\frac{dN_{corr}}{dp_T} = N_{seed} \times P_{B3} \times C_0 \int_{p_T - \sigma_{DC}}^{p_T + \sigma_{DC}} \frac{dN_{SIG}}{dp_T} dp_T \tag{5.13}$$

where N_{seed} is the number of off-vertex central arm tracks. P_{B3} is the probability that the central arm track projection lands within the spatial position of the search window in B3. Lastly, $C_0 \int \frac{dN_{SIG}}{dp_T} dp_T$ is the number of true charged hadron tracks with the same p_T and thus azimuthal angle as the candidate central arm track within the drift chamber resolution. P_{B3} has already been calculated above for the uncorrelated case in section 5.3.2 and is numerically the same for the correlated case. The other terms in equation 5.13 are plotted in figure 5-9 and shown in table 5.12. Their calculation will be discussed below.

5.5 Seed Tracks

The sample of candidate central arm tracks N_{seed} which constitute the fake SVXCNT sample in the correlated case are the off-vertex drift chamber tracks matched to the EMC and PC3.

Uncorrected Spectrum of EMC & PC3 Matched DC Tracks

Legend:
- ■ EMC & PC3 Matched DC Trks
- — Fit Signal + Background
- — Background Fit $\equiv \dfrac{dN_{BG}}{dp_T}$
- --- Normalizd Signal Fit $\equiv C_0 \dfrac{dN_{SIG}}{dp_T}$
- — Signal Fit $\equiv \dfrac{dN_{SIG}}{dp_T}$
- ∗ $C_0 \displaystyle\int_{p_T - \sigma_{DC}}^{p_T + \sigma_{DC}} \dfrac{dN_{SIG}}{dp_T} dp_T$
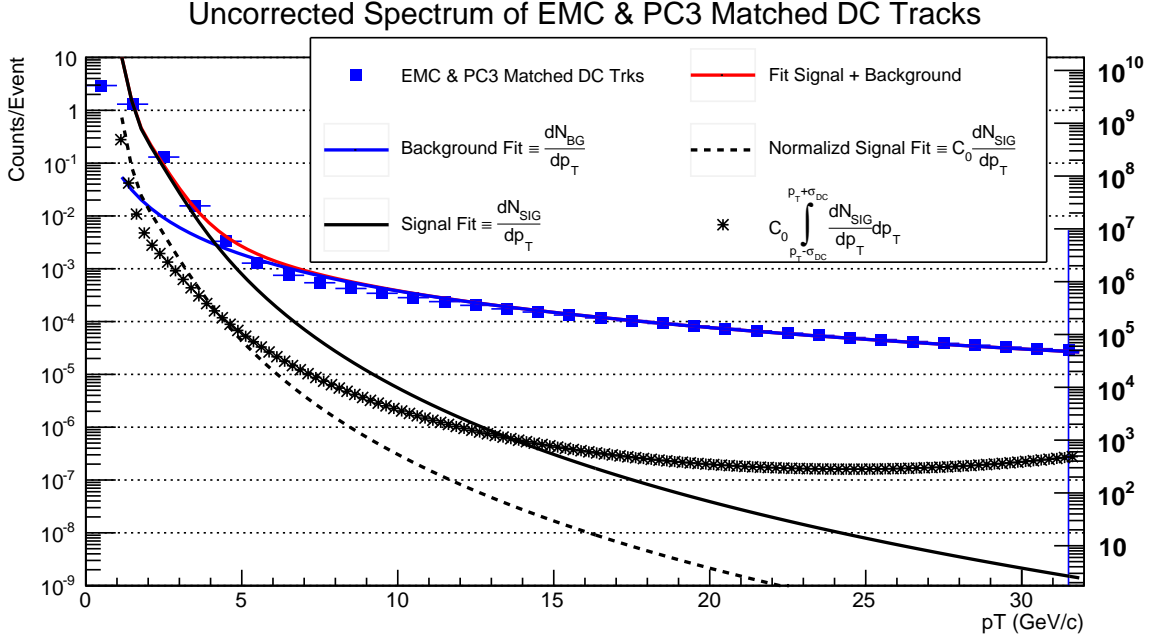
Figure 5-9: Spectrum of drift chamber tracks matched to the EMC and PC3 (as in fig. 5-2). Tracks are fit to a model of the signal (black curve), a model of the background (blue curve), and their sum (red curve). The signal is then normalized by the number of VTX standalone tracks in the central arm acceptance (black dotted line), to model the spectrum of real charged hadrons leaving correlated hits in the VTX. Finally these tracks are smeared by the drift chamber resolution (black stars).

These are off-vertex background tracks which have passed all of the central arm analysis cuts besides the cuts in the VTX. This is the same sample as in the uncorrelated case (N_{seed}) which have been calculated in section 5.3.1 above and are plotted again in figure 5-9. As in section 5.3.1, all central arm match tracks are plotted as blue closed squares, the total fit as a solid red line, the extracted charge hadron signal as a solid black line and the extracted background (N_{seed}) as a solid blue line.

5.6   Angular Matching

To randomly match an off-vertex central arm track with a set of correlated hits in the VTX from a real charged hadron, the real charged hadron must match in sign, spatial position

p_T	N_{seed}	$2\sigma_{p_T}$	$C_0 \int \frac{dN_{SIG}}{dp_T} dp_T$	P_{B3}	$\frac{dN_{corr}}{dp_T}$
1.625	0.00624129	[0.125]	0.197048	0.017794	4.80835e-06
5.125	0.000441578	[0.627813]	0.000960169	0.012628	1.17643e-09
10.125	9.21831e-05	[2.25281]	3.68788e-05	0.013202	9.86151e-12
15.125	3.66197e-05	[4.87781]	7.63498e-06	0.010906	6.69983e-13
20.125	1.89848e-05	[8.50281]	3.56306e-06	0.010906	1.62095e-13

Table 5.12: Terms of equation 5.13 for 5 example p_T bins.

and in angle. The probability of matching in spatial position is taken care of by P_{B3} above. Since angular information is already encoded in the drift chamber momentum measurement, the number of real charged hadrons in the VTX with the same angle as the projection of the central arm candidate is the number of charged hadrons with the same p_T within the momentum resolution of the drift chamber. To measure these charged hadrons, the functional form of the charged hadron spectrum is found by the full VTX DCA charged hadron analysis as in figure 5-1 and as the black curve in figure 5-9. The charged hadron spectrum is then normalized to C_0 which is $\frac{1}{2}$ of the number of standalone VTX tracks inside of the central arm acceptance. The factor $\frac{1}{2}$ is to take into account that only tracks with the same p_T and charge will have the same angle. The normalized curve is shown as a dashed black line on figure 5-9. Off-vertex central arm tracks can be randomly matched to real charged hadrons as long as they have a p_T within the drift chamber momentum resolution:

$$\frac{\delta p}{p} = 0.7\% \oplus 1.0\% \times p(\text{GeV/c}) \tag{5.14}$$

The normalized charged hadron signal smeared by the DC resolution is shown in figure 5-9 as black stars.
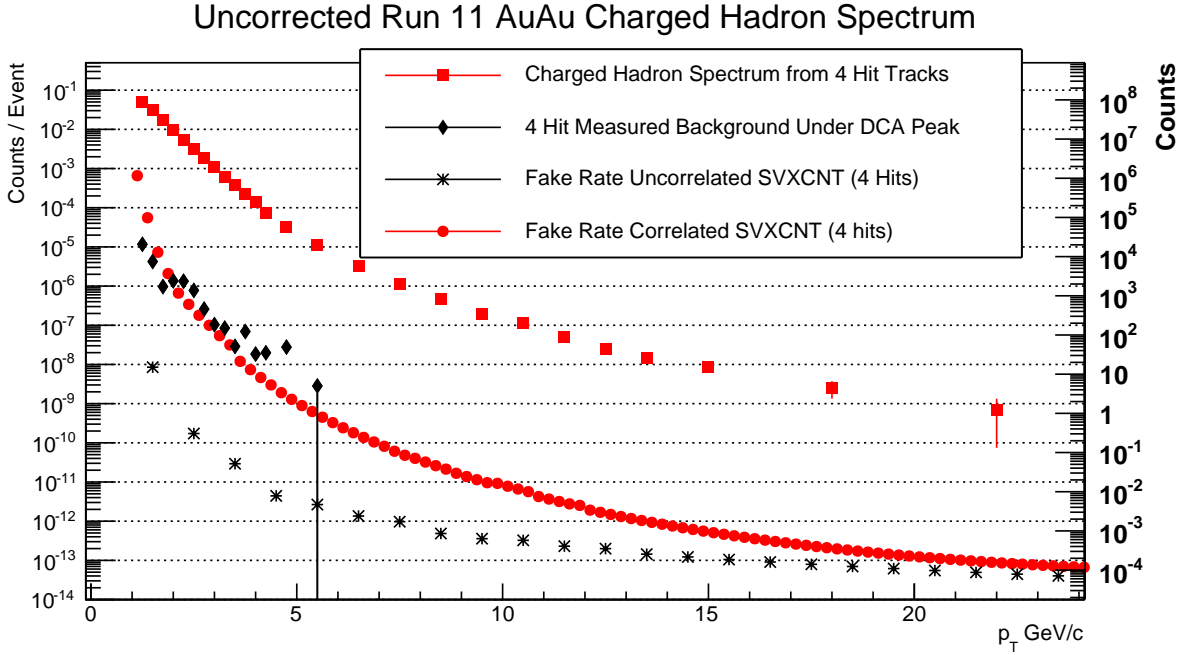
Figure 5-10: Comparison of uncorrected charged hadron yield to estimated spectrum of off-vertex central arm tracks randomly associated to tracks in the VTX. Uncorrected yield of charged hadrons (red squares) as well as the background remaining under the DCA peak (black diamonds) are shown along side the estimate of correlated background (red circles) and uncorrelated background (black stars).

5.7 Final Correlated Background Spectrum

The final spectrum of fake SVXCNT tracks due to matching off-vertex central arm tracks to random tracks in the VTX is shown in figure 5-10 as red circles. This spectrum appears to contribute significantly to the remaining background as measured under the DCA peak.

In conclusion, a significant fraction of the background remaining under the DCA peak after the Run-11 VTX charged hadron analysis is due to random combinations of off-vertex central arm tracks with tracks in the VTX. As seen in figure 5-10 the estimate of correlated background tracks closely resembles the shape of the remaining background. Because of their similar shapes, it is reasonable to extrapolate the estimated background level to high p_T. This is shown in figure 5-11, where the charged hadron signal spectrum is found by

fitting the results of the VTX DCA analysis to equation 5.6 as in section 5.3.1 above. The background spectrum has been extended to high p_T, by summing the contributions from random VTX hits and random VTX tracks and scaling up by 2.76 to level of background measured under the DCA peak. The background was then fit to a spline polynomial and extrapolated to high p_T. It is observed that the signal spectrum will intersect the spectrum of inherent VTX background at 46.9 GeV/c. Above 46.9 GeV/c the signal to background ratio will be less than 1. On average, producing a single charged hadron at 46.9 GeV/c would take 2×10^9 events [3]. Approximating the efficiency of SVXCNT tracks as 1/38.38 from fit parameter p7 in table 5.3, on average it would take 7.7×10^{10} events to obtain a single track at 46.9 GeV/c. This is about 50 times the statistics used in Run-11.

5.8 Estimate of the Background Rate Increase For 3 Hit tracks

As discussed above, this analysis was performed with 4 hit tracks. However, the effective acceptance of the VTX detector greatly increases if 3 hit tracks are used instead. In this section, we will estimate the increase in background tracks caused by accepting 3 hit tracks instead of 4 hit tracks.

5.9 Uncorrelated Background from Random Association of Hits (3 Hit Tracks)

As in the 4 hit case, the rate of fake SVXCNT tracks matched to 3 random hits from 3 independent tracks, in the VTX can be calculated by considering the tracking algorithm search window size needed to accommodate multiple scattering the drift chamber angular
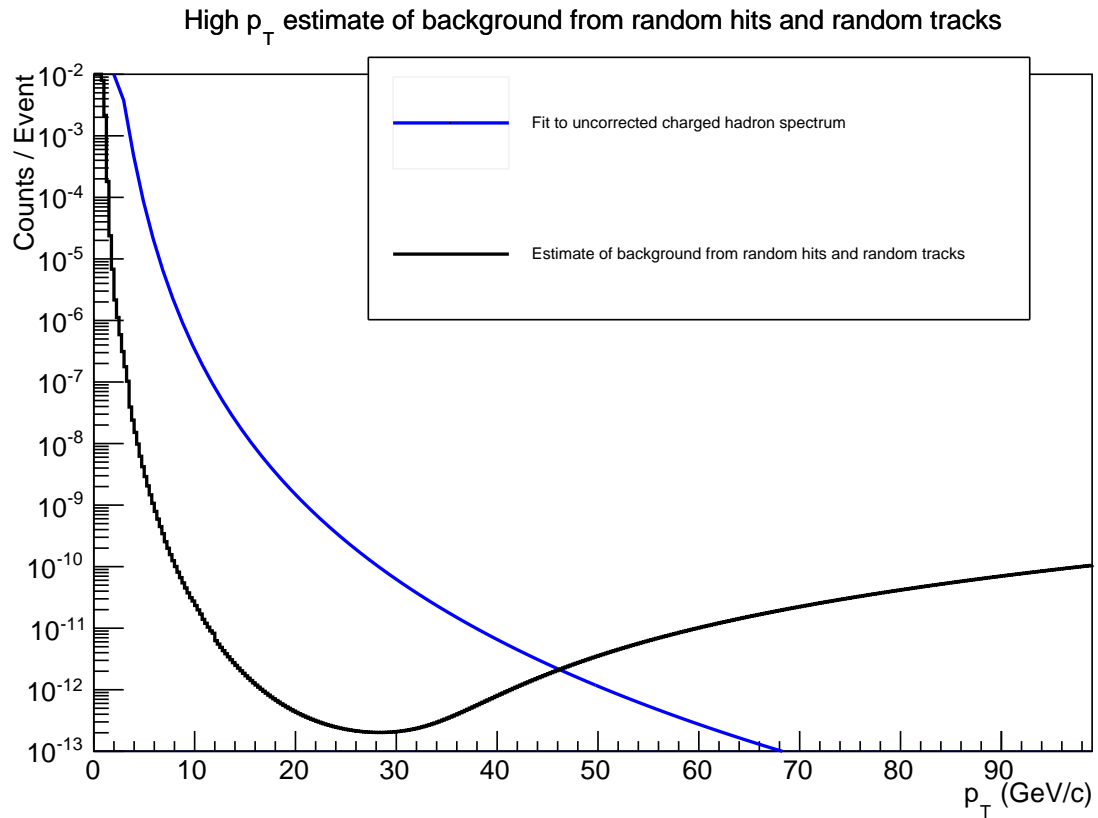
Figure 5-11: Extrapolation of charged hadron spectrum (blue) and background estimate (black) to very high p_T. The charged hadron spectrum is found by fitting the results of the VTX DCA analysis to equation 5.6. The background spectrum has been obtained by summing the contributions from random VTX hits and random VTX tracks, scaling up by a factor 2.76 to the level of background measured under the DCA peak and fit to a polynomial spline.

resolution. As above in equation 5.1 (5.15), the probability of reconstructing such a track is:

$$P(\text{Uncorrelated}) = N_{seed} \times \prod_{i=1}^{3} P_i \qquad (5.15)$$

Where N_{seed} is the number of off-vertex central arm tracks, and P_i is the probability of a random hit falling within the search window for a particular VTX layer i. Thus, the effect of downgrading to 3 hit tracks will mainly be felt in the loss of one of the inner layer probabilities, either P_2 or P_3. As calculated above and shown in table 5.11, this will affect a loss in rejection power of either 0.32% or 0.23% depending on whether the missing hit is in layer 2 or layer 3. A 3 hit SVXCNT track can be formed from either layers 0,1,2 or layers 0,1,3. Both possibilities are considered and their probabilities are combined in what follows. The spectrum of fake 3 hit SVXCNT tracks from random hits is shown in figure 5-12. For comparison, the DCA analysis described in the preceding chapters has been repeated for 3 hit SVXCNT tracks. The unccorrected p_T spectrum resulting from that analysis is also shown along side the results of the 4 hit analysis infigure 5-12. As with 4 hit tracks, at low p_T the estimate of fake tracks from random hits significantly underestimates the background as measured under the DCA peak. However, for 3 hit tracks at high p_T the estimate matches the measured background estimate well.

5.10 Background From Random VTX Tracks (3 Hit Tracks)

The estimated rate of reconstructing fake tracks by matching an off-vertex central arm track with a real charged hadrons passing through the VTX is given by 5.16:

$$\frac{dN_{corr}}{dp_T} = N_{seed} \times P_{outer} \times C_0 \int_{p_T - \sigma_{DC}}^{p_T + \sigma_{DC}} \frac{dN_{SIG}}{dp_T} dp_T \qquad (5.16)$$
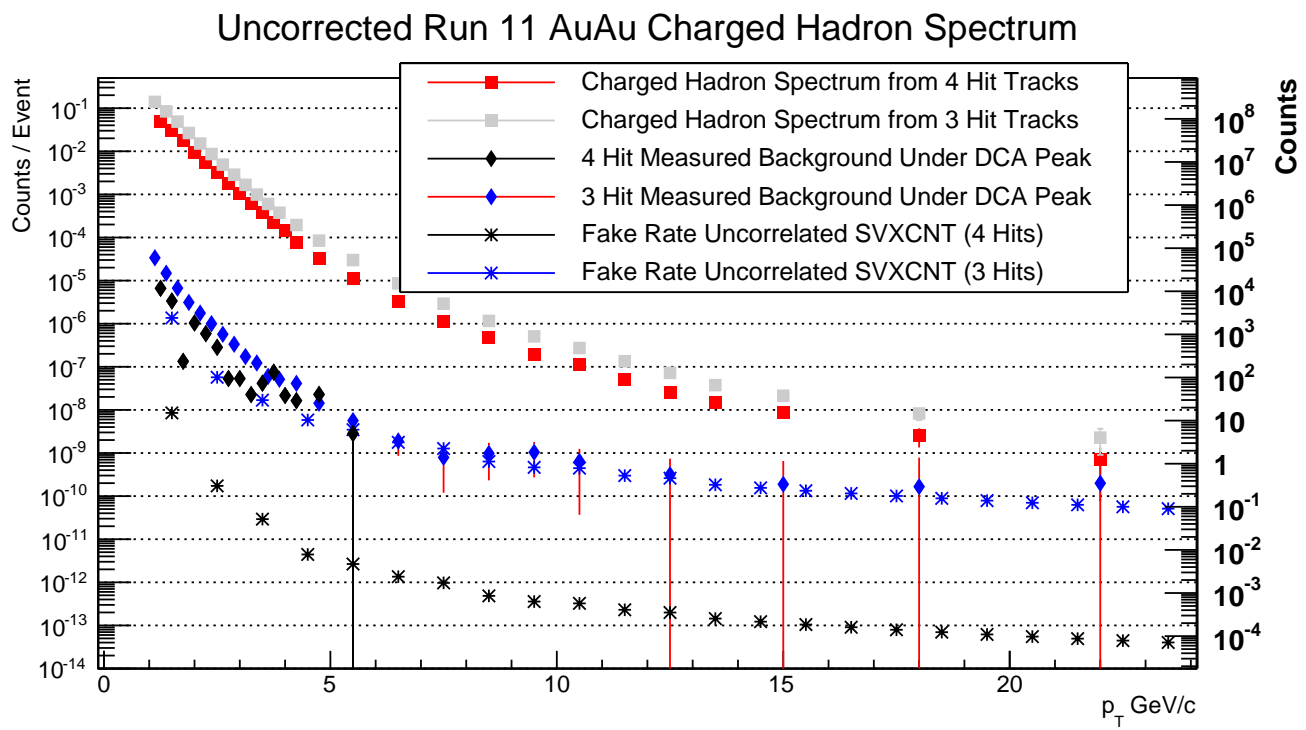
Figure 5-12: Uncorrected spectra (squares) shown alongside the background measured under the DCA peak (diamonds) compared to the calculated estimate of fake tracks from random VTX hits (stars) for both 3 and 4 hit tracks.
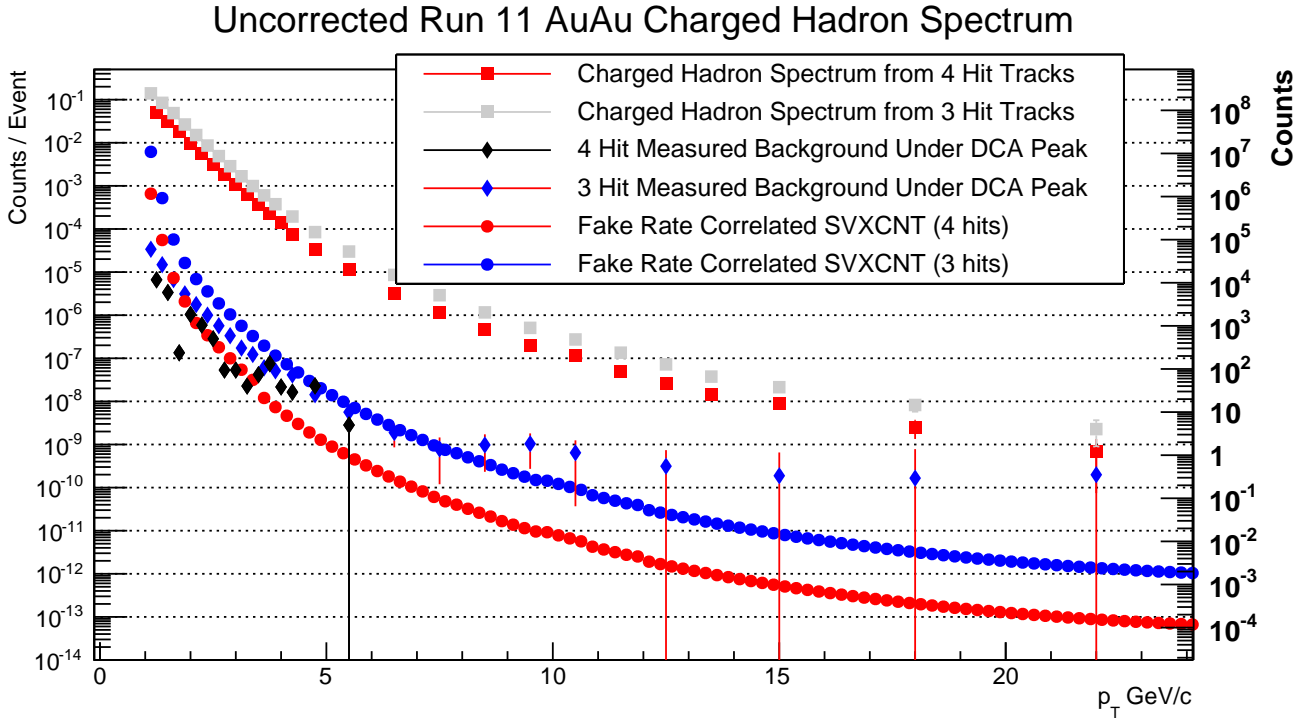
Figure 5-13: Uncorrected spectra (squares) shown alongside the background measured under the DCA peak (diamonds) compared to the calculated estimate of fake tracks from random VTX tracks (stars) for both 3 and 4 hit tracks.

Where P_{outer} is the probability that the central arm tracks points within the search window on the outermost layer (either layer 2 or 3). P_{outer} is multiplied by the number of seed tracks and the number of available real charged hadrons in the VTX with the same p_T (or angle) as the misreconstructed p_T of the off-vertex central arm track (within the momentum resolution of the drift chamber). This last term is normalized by the number of standalone tracks which have 3 hits in the VTX. The change in this normalization factor contributes most when switching from 4 to 3 hit tracks, as there are many more fully reconstructed 3 hit standalone VTX tracks compared to 4 hit standalone VTX tracks.

The effect on the number of random matches to real tracks in the VTX of downgrading to 3 hit tracks is shown in figure 5-13. Here, altough the a prioi estimate of fake tracks overestimates the measured background at low p_T, it exhibits a similar shape. It appears,

that for 3 hit tracks, the low p_T background is due to off-vertex central arm tracks associated with correlated hits (a track) in the VTX and the remaing background at high p_T is due to the association to random uncorrelated hits.

5.11 Conclusions after Estimating the Background Present in 3 Hit Tracks

In conclusion, the methods described here for estimating a priori the fake rate of SVXCNT tracks, survive the jump form 4 hit SVXCNT tracks to 3 hit SVXCNT tracks. The total fake rate spectra, formed by summing the contributions from random tracks and random independent hits is shown in figure 5-14. The unccorrected charge hadron spectra for both 3 and 4 hit tracks are shown. Here one can observe that using 3 hit tracks instead of 4 hit tracks improves the effective acceptance of the VTX by a factor ~ 3. However, using 3 hit tracks reduces the rejection power of the VTX by almost 3 orders of magnitude. Therefore, we have chosen to require that SVXCNT tracks have 4 hits in the VTX for this analysis.
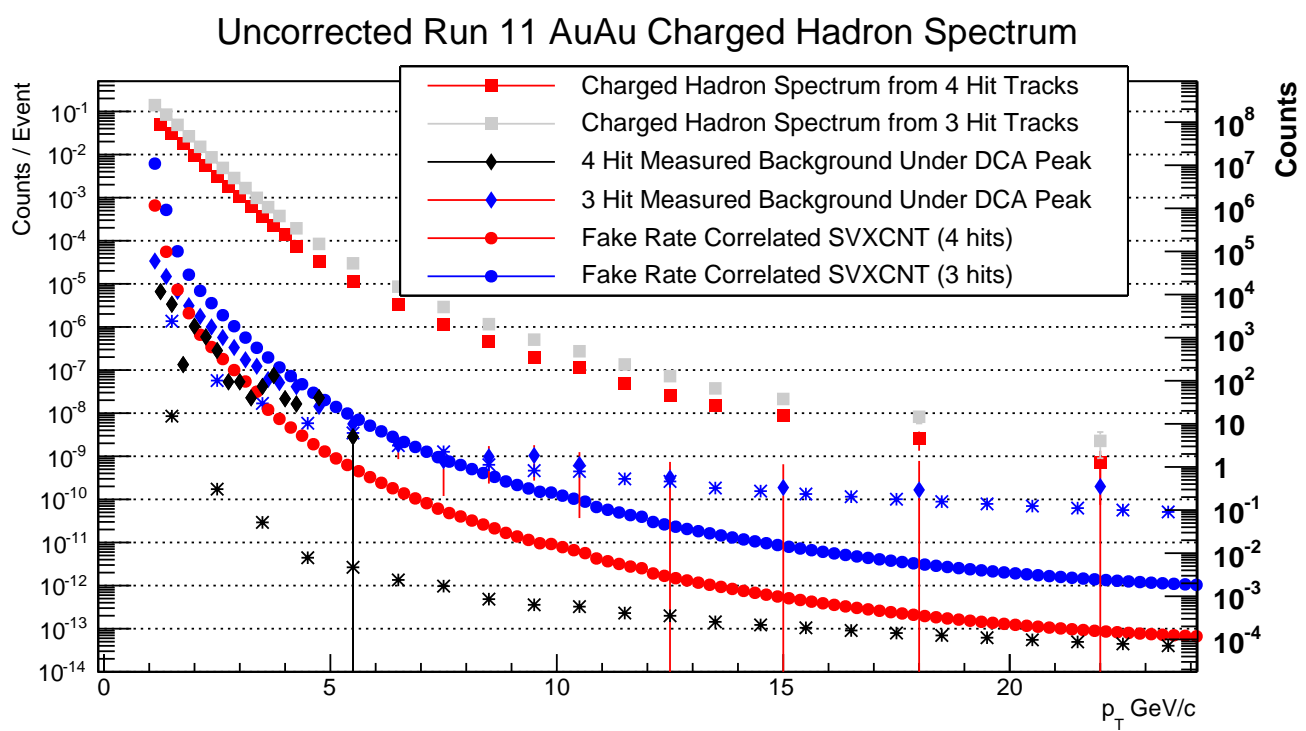
Figure 5-14: Uncorrected charged hadron spectra compared to the final sum of estimated fake tracks from random hits and random tracks in the VTX.

Chapter 6

Spectra

6.1 Uncorrected Spectrum

The uncorrected spectrum of charge hadrons is found by taking the DCA distributions of each p_T bin and integrating over $\pm 2\sigma$ of the Gaussian DCA peak after the DCA analysis described above. This results in the uncorrected spectrum shown in figure 6-1.

6.2 Corrected Spectrum

The uncorrected spectrum is made invariant by dividing by $2\pi p_T$. Then the spectrum is corrected by correcting for acceptance and efficiency and for the bin shift effect.

6.2.1 Efficiency Correction

The p_T dependent acceptance and efficiency is calculated using Monte Carlo simulations. A flat spectrum of single charged pions is generated by PYTHIA simulations and passed through a GEANT reproduction of the full PHENIX detector including hot and dead maps. The GEANT simulation simulates the responses of each detector to the simulated particle.
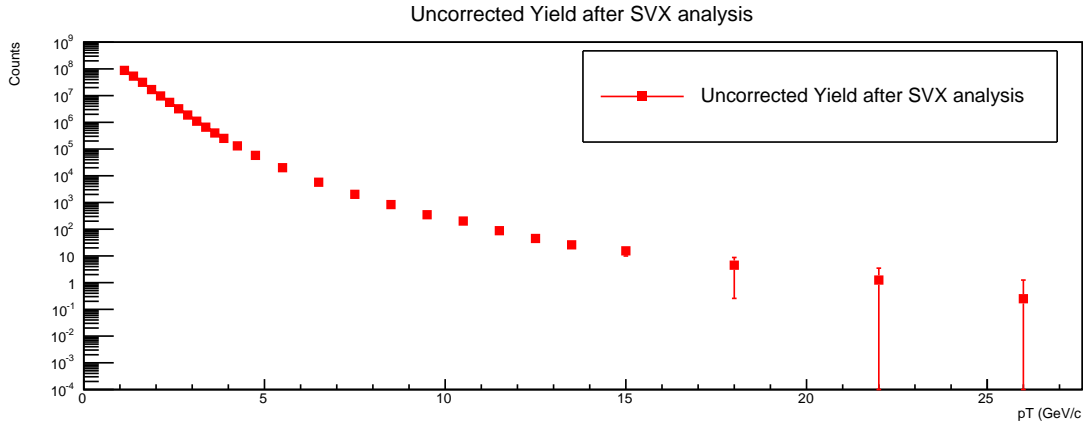
Figure 6-1: Uncorrected charged hadron spectrum.

Effects from decays and multiple scattering are also taken into account.

The effect of efficiency on the p_T spectrum is studied by weighting the flat input p_T spectrum by the expected charged hadron spectrum. Finding the expected spectrum is done iteratively. First the full VTX analysis is run on the data. As in the PHENIX π_0 analysis [27], the invariant yield from this first run of the analysis is fit to $f_0(p_T)$, a Hagedorn at low p_T with a Woods-Saxon transition to a power law at high p_T, as in equation 6.3 and 6.4.

The fit is as shown in figure 6-2. The Monte Carlo simulation is then run using this fit as the weight for the MC p_T spectrum. An efficiency ϵ_0 is calculated by finding the ratio of the p_T spectrum after the full analysis divided by the spectrum of the PYTHIA input particles. The VTX charged hadron analysis is run again, this time corrected by ϵ_0. The corrected invariant yield is again fit to a Hagedorn/power law $f_1(p_T)$. The simulations are rerun using $f_1(p_T)$ as the p_T weight function. This procedure is performed until the efficiency functions converge.

6.2.2 Occupancy Efficiency

The efficiency calculated in the previous section is the efficiency of reconstructing a single track. There is an additional efficiency loss when simultaneously reconstructing many tracks

70
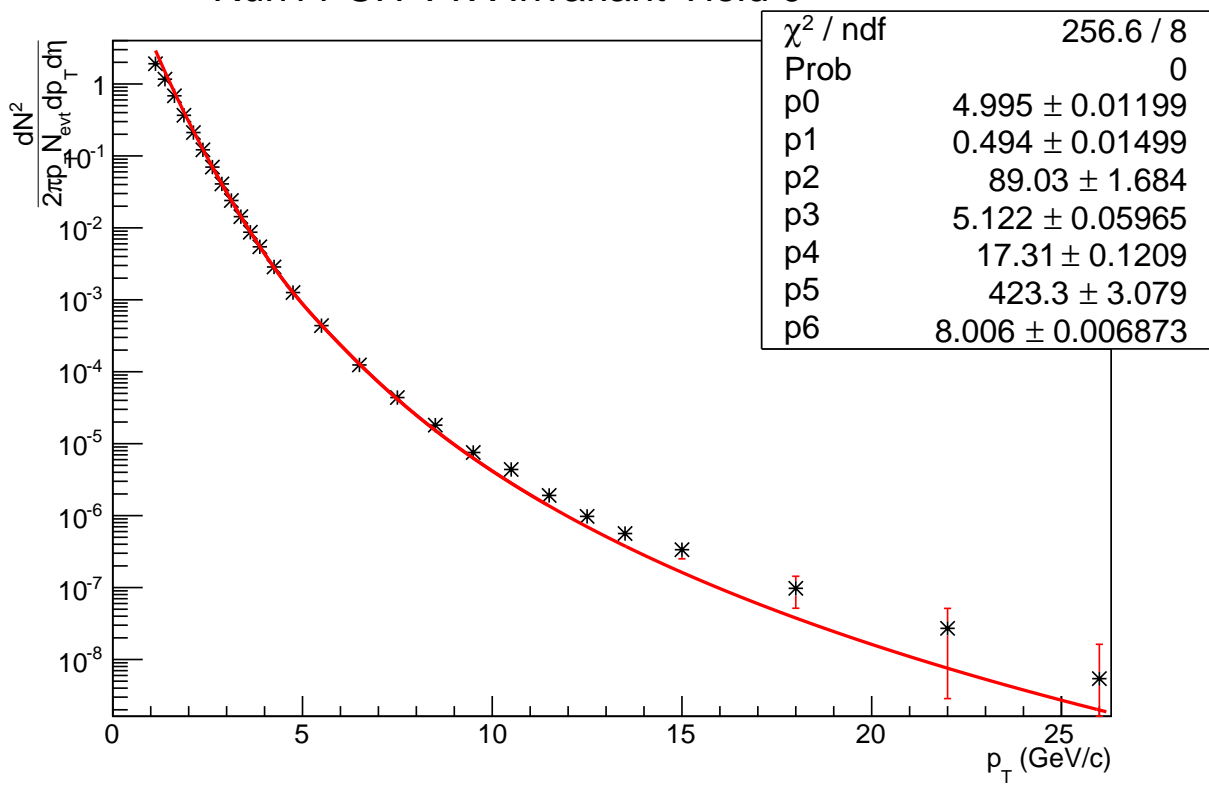
Figure 6-2: Charged hadron invariant yield after first iteration of the efficiency correction. Invariant yield is fit to a Hagedorn at low p_T with a Woods-Saxon transition to a power law at high p_T.
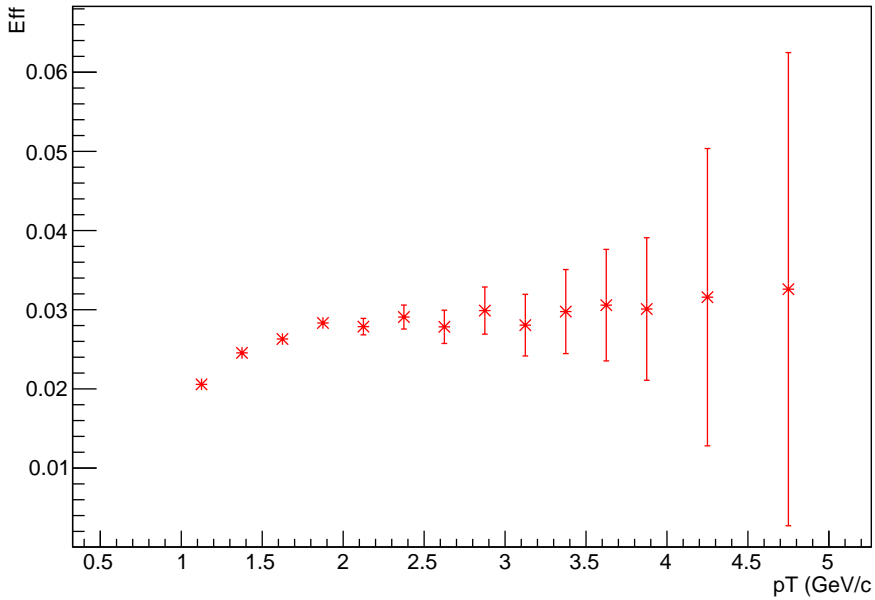
Figure 6-3: Simulated efficiency of the Run-11 VTX charged hadron analysis

in a high multiplicity event from spacepoints in each tracking layer. A correction factor for this effect in the PHENIX central arms has been measured previously and is shown as a function of the number of collision participants N_{Part} in figure [8].

6.2.3   Bin Shift Correction

A correction must be applied to account for the finite bin size used to plot the spectrum. Since the spectrum is steeply falling, the points obtained by integrating over the DCA peaks in each p_T bin are artificially enhanced when placed in the middle of each p_T bin. This effect can be corrected for by either shifting the points horizontally in the p_T direction or shifting the points vertically along the invariant yield direction. The latter procedure will be pursued here.

To correct for the bin shift, first a local exponential fit $c_0 e^{c_1 p_T}$ is performed in the vicinity
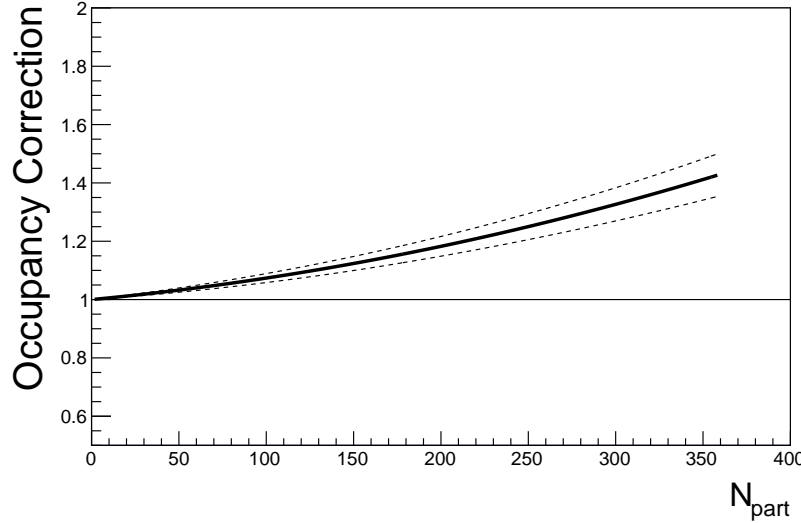
Figure 6-4: Occupancy correction per number of participants N_{Part} as previously measured by PHENIX [8].

around each point. The point is then corrected by the integral of the fit:

$$
\mathrm{Yield}_{\mathrm{out}}(p_T) = \frac{c_0 e^{c_1 p_T}}{\frac{1}{b} \int\limits_{p_T - b/2}^{p_T + b/2} c_0 e^{c_1 p_T'} dp_T'} \mathrm{Yield}_{\mathrm{in}}(p_T) \tag{6.1}
$$

where b is the bin width and c_0 and c_1 are constants found by the fit.

The invariant fits before and after the bin shift correction are shown in figure 6-5. The discontinuous sawtooth behavior is due to the nonuniform bin widths used in the DCA analysis (see section 4.0.3). Bins with large widths will have a larger correction.

6.2.4 Comparison to Previous Measurements

To compare to previous measurements, the invariant charged hadron yield corrected with the simulated efficiency (figure 6-3) is divided by a fit to the published charged hadron spectrum[8]. This ratio is shown in the bottom panel of figure 6-6 and enlarged in figure
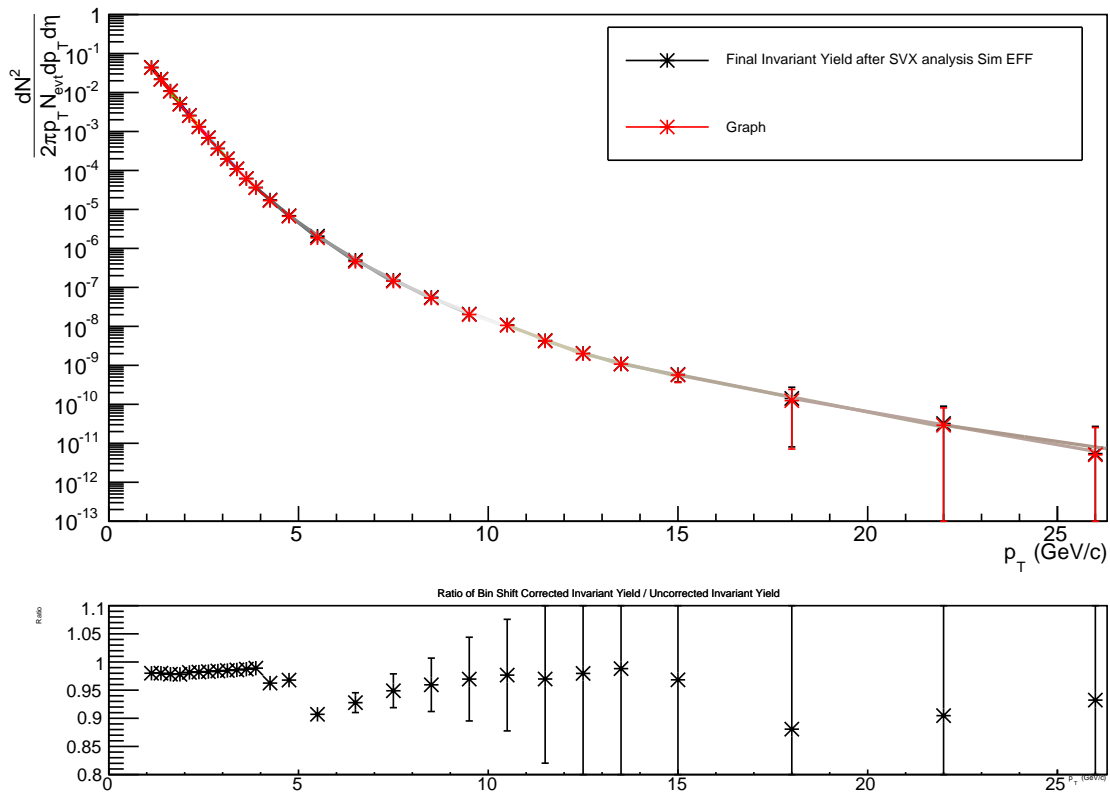
Figure 6-5: Bin shift correction. Top: Invariant yield before (black) and after (red) bin shift correction. Bottom: Ratio of invariant yield after bin shift correction to invariant yield before bin shift correction.

χ^2 / ndf	6.657 / 8
Prob	0.5741
p0	4.999 ± 0.7648
p1	0.02035 ± 0.008249
p2	43.53 ± 0.01642
p3	4.863 ± 0.0002161
p4	17.88 ± 0.0005853
p5	62.41 ± 0.05974
p6	8.159 ± 0.0005338
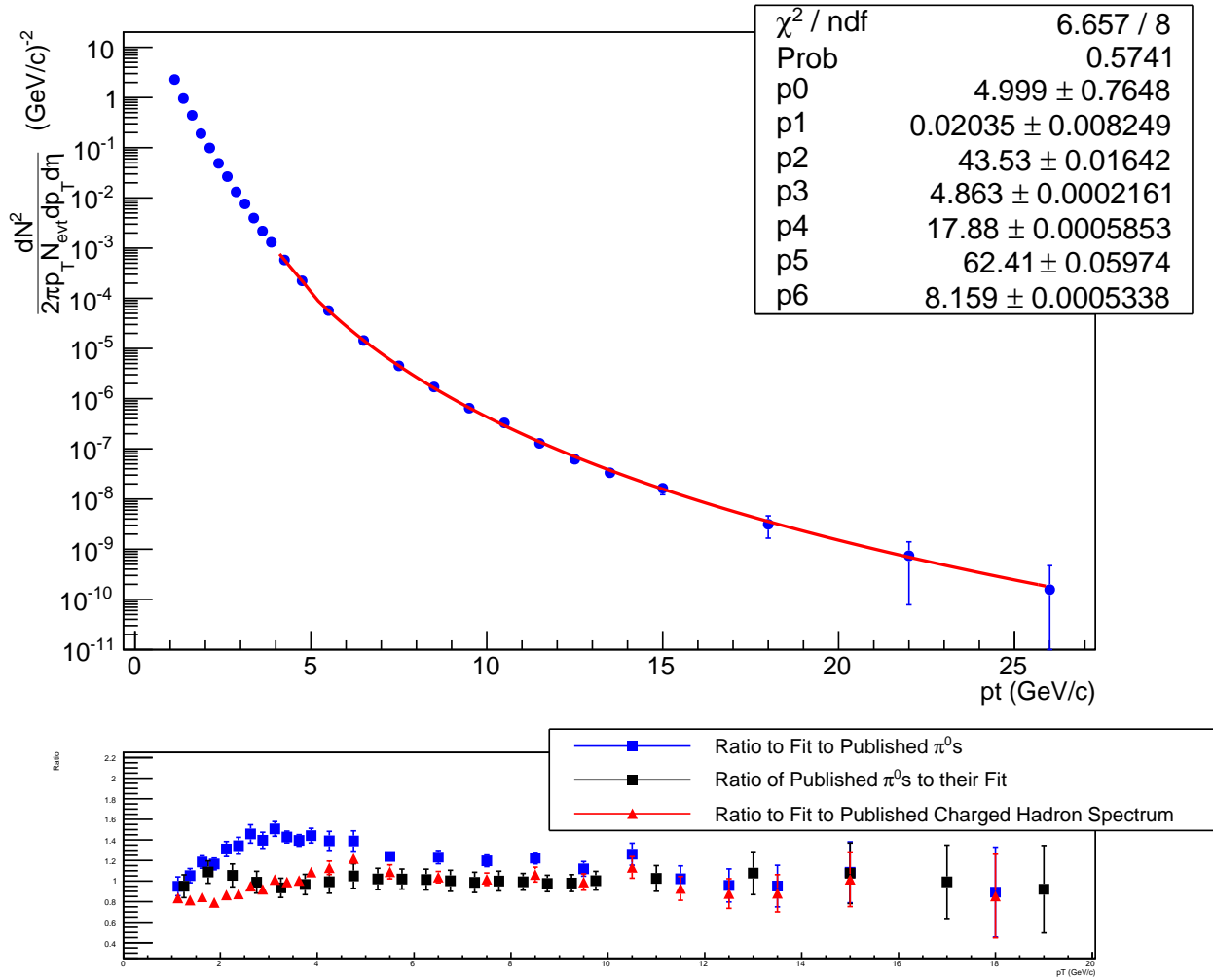
Figure 6-6: Top: Work in progress charged hadron spectrum from RUN-11 after VTX analysis, corrected by the simulated detector efficiency. Bottom: Comparison of Run-11 VTX charged hadron spectrum to published charged hadron measurement [8] and π_0 spectrum [7], [2].
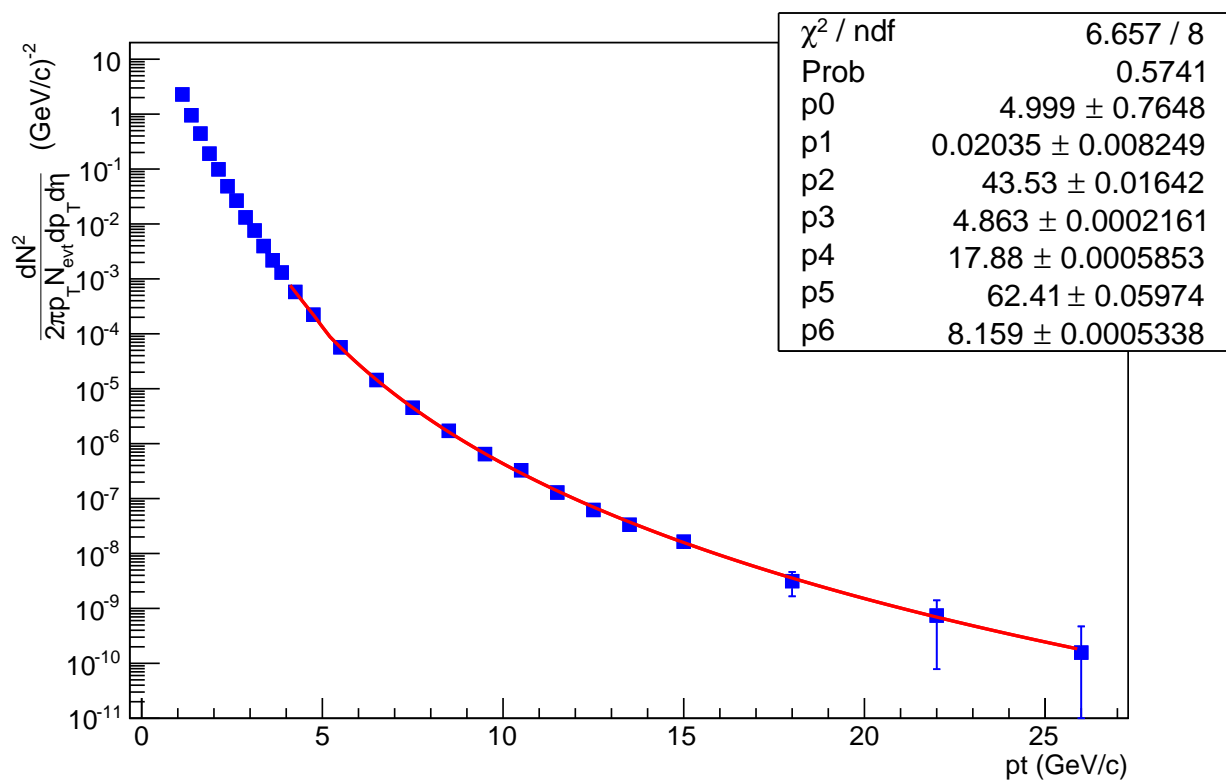
Figure 6-7: Work in progress charged hadron spectrum, which has been corrected by the simulated detector efficiency, is fit to a Hagedorn function at low p_T with a Woods-Saxon transition to a power law at high p_T.
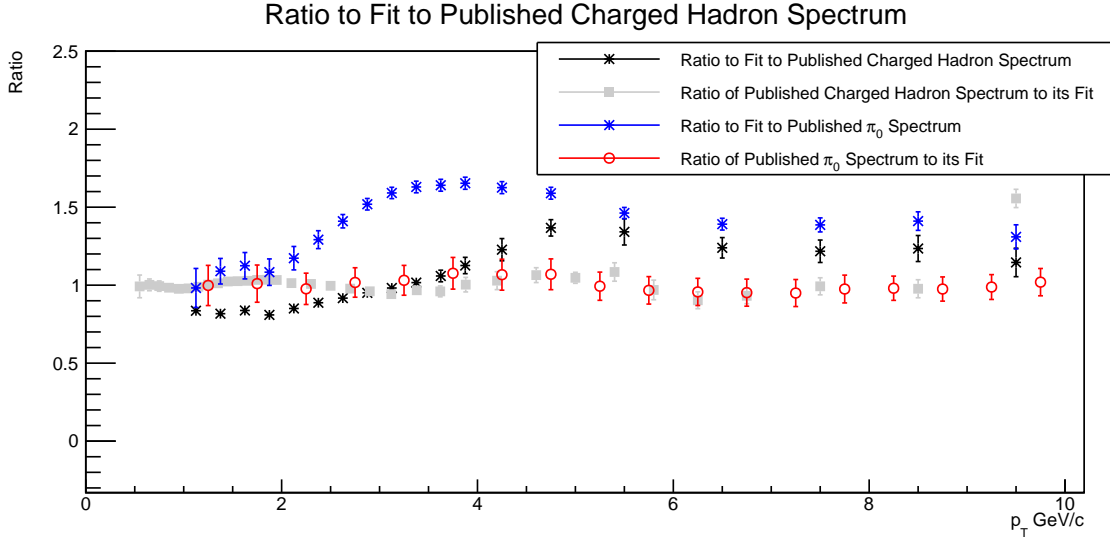
Figure 6-8: Ratio of Run-11 VTX charged hadron spectrum to fits to published charged hadron spectrum (Black Stars) [8] and π_0 spectrum (Blue Stars)[7], [2]. Also shown, are the ratios of the published charged spectrum to its fit (Gray Squares) and the published π_0 spectrum to its fit (Red Circles).

6-8. Also shown, is the ratio to a fit to the published spectrum of neutral pions[7], [2]. If the simulated efficiency were functioning correctly, the ratio to the published charged hadron spectrum would be unity within uncertainties where the two spectra overlap in momentum range from 1 GeV/c to 9.5 GeV/c. Instead, the ratio appears to be flat above 5 GeV/c, but exhibits a p_T dependent shape at low p_T. Due to hardware problems of the detector in its first year of operation, the acceptance was fluctuating significantly. This makes it challenging to calculate an absolute efficiency at low p_T and may explain the discrepancy to the previous measurement.

6.2.5   Low p_T Correction

As high momentum tracks become very straight compared to low momentum tracks which have a greater bend in the magnetic field, the detector tracking efficiency becomes independent of p_T at large momenta. The low p_T anomaly can therefore be corrected for, by

bootstrapping the efficiency at low p_T to the published hadron spectrum, without losing the information gained from the VTX analysis about the spectrum's shape at high p_T. This is done first by finding the ratio of the charged hadron invariant yield from the VTX analysis without efficiency correction and dividing by the published charged hadron spectrum. This ratio is shown in figure 6-9 for minimum bias events and in figure 6-10 for events in the 60-93% centrality class. As expected, the ratio exhibits a p_T dependent shape at low p_T and is flatter at high p_T. This behavior is parameterized by fitting the ratio to a constant minus an exponential, such that in the high p_T region the uncorrected spectrum is scaled by a constant. The fit is performed in the region below 7.5 GeV/c, so that it is constrained by data in the region of overlap between the two analyses. The exponential componant of the fit is also constrained to be fully decayed by 8 GeV/c to insure that the spectrum's shape is not modified at high p_T. This is done by first fitting the ratio to a constant between $5.0 < p_T < 8.0$ (GeV/c). The results of this fit are shown in table 6.1 for both minium bias and the 60-93% centrality class. The ratios are then fit to equation 6.2, with the constant parameter constrained to the value of the constant fit within the errors of that fit.

$$R_{\mathrm{EFF}} = C_0 - C_1 e^{C_2 p_T} \tag{6.2}$$

Centrality Class	Constant	Error
Min. Bias.	4.75216e-02	7.07098e-04
60-93%	3.98931e-02	8.41618e-03

Table 6.1: Parameters of a constant fit to the ratio of the VTX analysis to the published charged hadron spectrum for min bias as well as the 60-93% most central, fit within $5.0 < p_T < 8.0$ (GeV/c).

Correcting the charged hadron spectrum from the VTX analysis with R_{EFF} produces the invariant yield shown in figure 6-11. Here, the bootstrapped efficiency was also used to

	Min Bias		60 - 93 % Central	
	Parameter	Error	Parameter	Error
C_0	4.68145e-02	6.61683e-06	3.14769e-02	7.20644e-05
C_1	-4.11774e-02	1.26230e-04	-2.96870e-02	5.73818e-04
C_2 (c/GeV)	-5.99491e-01	2.37815e-03	-6.82914e-01	1.52558e-02

Table 6.2: Parameters of the fit to the ratio of the VTX analysis to the published charged hadron spectrum for min bias as well as the 60-93% most central.

obtain the absolute normalization of the spectrum. As expected the ratio to the published charged hadron spectrum is unity, while the ratio to the published neutral pion spectrum is flat at high p_T.

6.2.6   Final Corrected Invariant Yield

The final spectrum after taking into account the various corrections discussed above is fit again to a Hagedorn at low p_T with a Woods-Saxon transition to a power law at high p_T. Both the spectra corrected by the simulated efficiency and the spectra corrected for by the bootstrapped efficiency are fitted to the same functions as shown in figures 6-7 and 6-12 respectively.

The fit function is:

$$f(p_T) = T(p_T)\frac{p_2}{(1 + p_T/p_3)_4^p} + (1 - T(p_T))\frac{p_5}{p_T^{p_6}} \tag{6.3}$$

where,

$$T(p_T) = \frac{1}{1 + e^{\frac{p_T - p_0}{p_1}}} \tag{6.4}$$
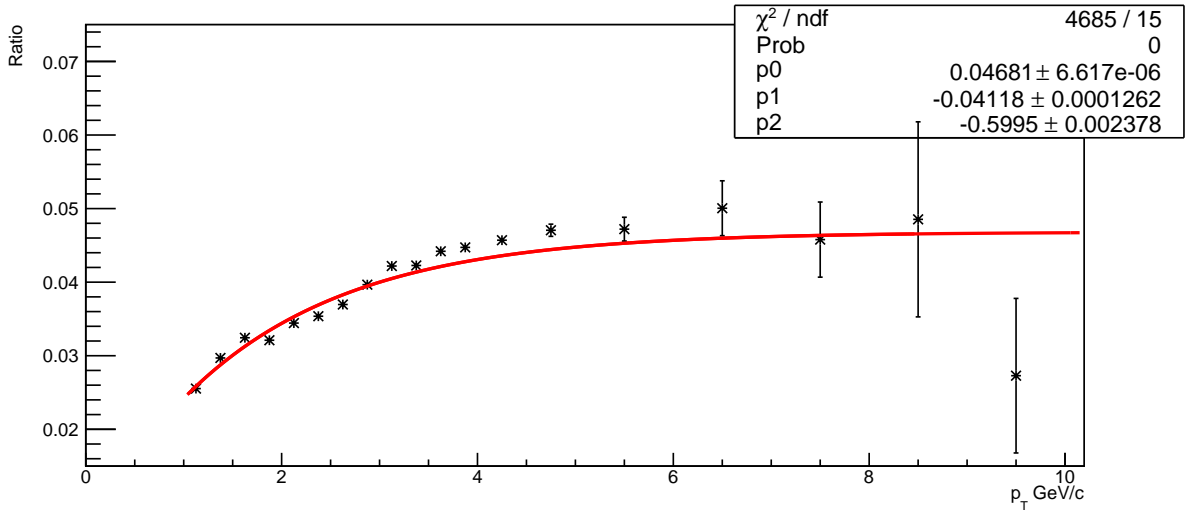
Figure 6-9: Ratio of Run-11 VTX charged hadron spectrum to fits to published charged hadron spectrum (Black Stars) [8], both for minimum bias events. The ratio is fit to a constant minus a decaying exponential, which models an efficiency that is highly p_T dependent at low p_T and p_T independent at high p_T.
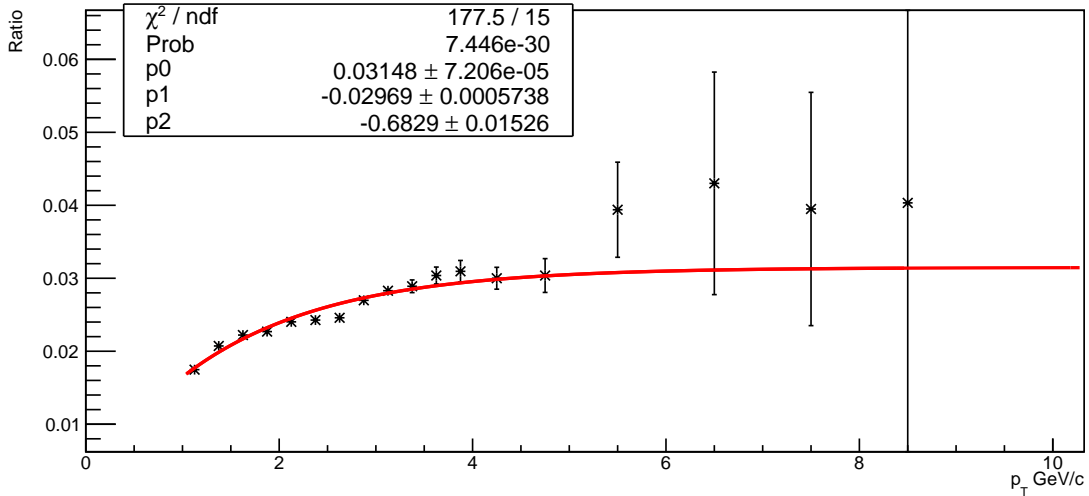
Figure 6-10: Ratio of Run-11 VTX charged hadron spectrum to fits to published charged hadron spectrum for events in the 60-93% centrality class [8].
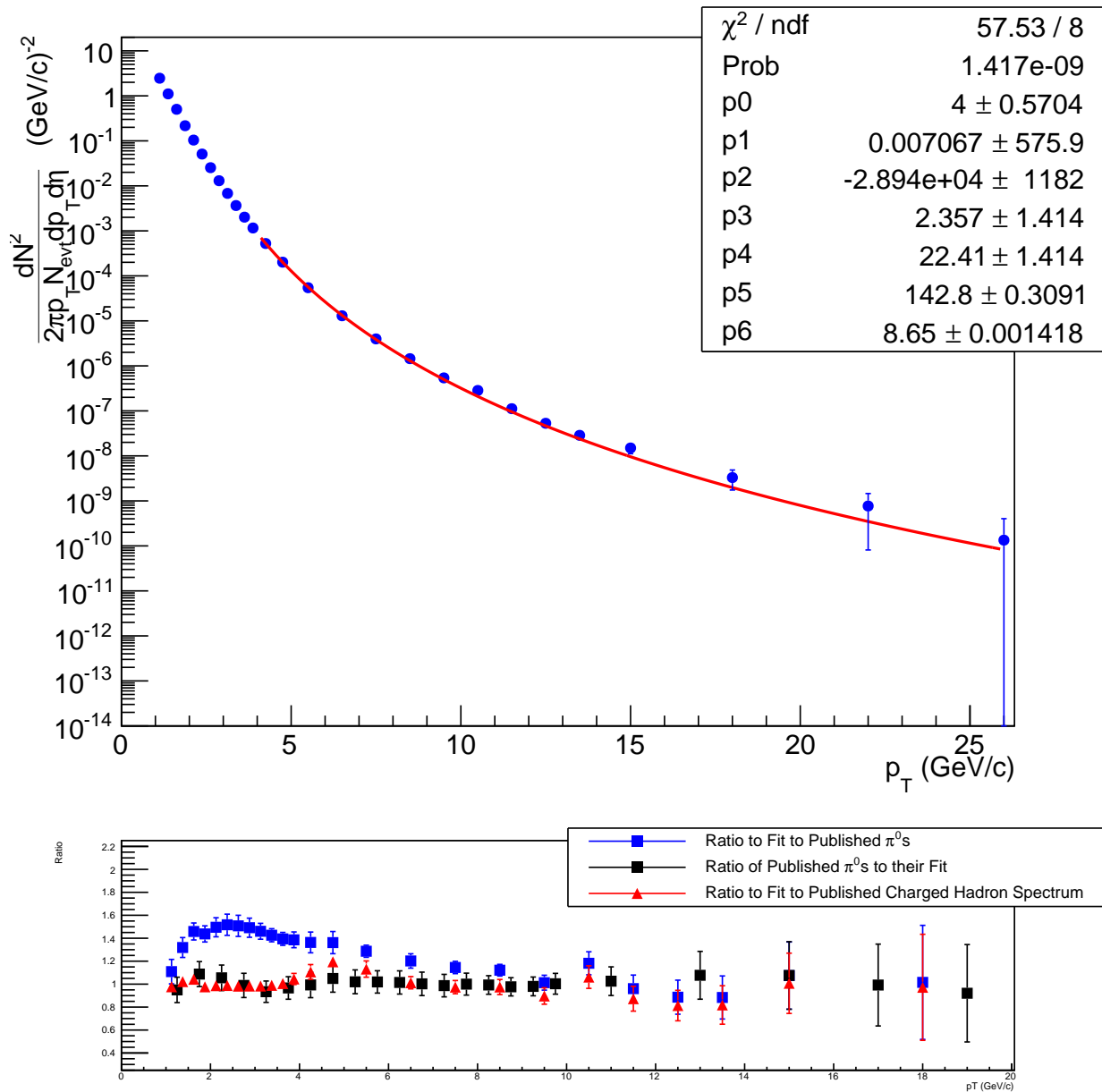
Figure 6-11: Top: Work in progress charged hadron spectrum from RUN-11 after VTX analysis, corrected by the bootstrapped detector efficiency. Bottom: Comparison of the spectrum to published charged hadron measurement [8] and π_0 spectrum [7], [2].
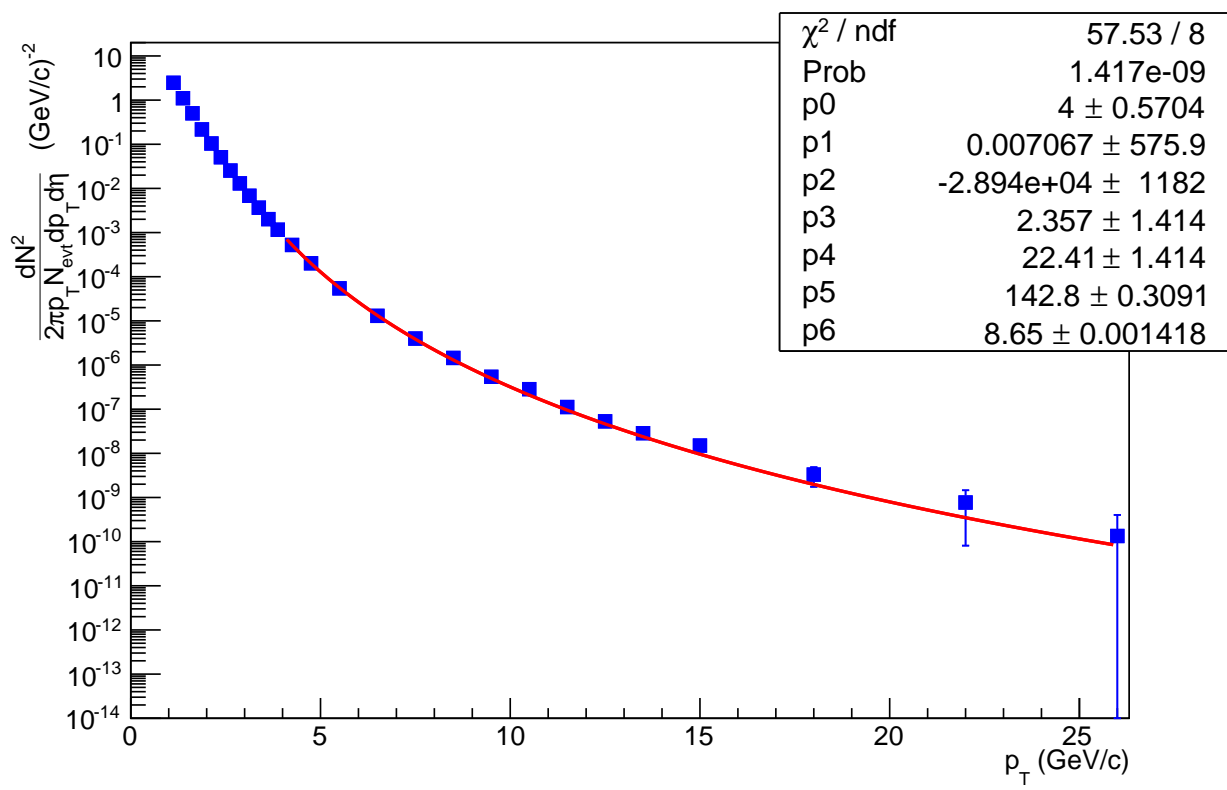
Figure 6-12: Work in progress charged hadron spectrum from RUN-11 after VTX analysis, corrected by the bootstrapped detector efficiency. Spectrum is fit to a Hagedorn function at low p_T with a Woods-Saxon transition to a power law at high p_T.

	Simulated Eff.		Bootstrapped Eff.	
	Parameter	Error	Parameter	Error
p_0 (GeV/c)	4.99903e+00	7.64787e-01	4.00024e+00	5.70352e-01
p_1 (GeV/c)	2.03513e-02	8.24926e-03	7.06739e-03	5.75877e+02
p_2 (mbarn GeV^{-2}/c^3)	4.35316e+01	1.64249e-02	-2.89427e+04	1.18241e+03
p_3 (GeV/c)	4.86310e+00	2.16085e-04	2.35693e+00	1.41421e+00
p_4	1.78790e+01	5.85254e-04	2.24106e+01	1.41421e+00
p_5 (mbarn GeV^{-2}/c^3)	6.24055e+01	5.97353e-02	1.42802e+02	3.09149e-01
p_6	8.15935e+00	5.33830e-04	8.65039e+00	1.41797e-03

Table 6.3: Parameters of the fit of the invariant yield of charged hadrons after applying the simulated detector efficiency compared to those found after applying the boot strapped efficiency.

6.2.7 Systematic Uncertainties

The main source of systematic uncertainty is uncertainty in the momentum resolution of the drift chamber. This uncertainty is estimated by running a Monte Carlo simulation of the drift chamber resolution smearing, while varying the momentum resolution. Varying the momentum resolution by uncertainty on the momentum resolution and studying the subsequent modification to the charged hadron spectrum yields the systematic errors shown in table 6.4.

p_T (GeV/c)	Relative Sys. Error (%)	p_T (GeV/c)	Sys. (%)	p_T (GeV/c)	Sys. (%)
1.5	0.048	8.5	1.80	15.5	5.34
2.5	0.060	9.5	2.06	16.5	6.11
3.5	0.41	10.5	2.72	18.0	6.81
4.5	0.57	11.5	2.93	22.0	10.01
5.5	0.87	12.5	3.56	26.0	13.24
6.5	1.11	13.5	3.86		
7.5	1.52	14.5	4.57		

Table 6.4: Systematic errors in the invariant charged hadron yield due to uncertainty in the momentum resolution.

Chapter 7

Ratio of Central to Peripheral Yields, R_{CP}

In order to measure the suppression of hard scattered partons as they traverse the strongly interacting medium, the modification of the produced particle's p_T spectrum with respect to a system in which no quark-gluon plasma can be made. Accordingly, in this analysis the modification of the charged hadron p_T spectrum will be measured with respect to peripheral collisions. When heavy ions collide, they collide with a distribution of impact parameters and consequently a varying amount of overlap of the colliding nuclei's nuclear wavefunctions. Events can be categorized into classes according to the degree to which the colliding ions overlap geometrically. This classification is known as centrality. In this analysis, we will compare the charged hadron spectrum for minimum bias events, collisions distributed across all centralities to peripheral events. Peripheral events, are collisions with minimal geometric overlap. In this class of collisions, there is a lower collision energy density and thus a lower probability of quark-gluon plasma formation.

Centrality Class	N_{COLL}	Sys. Err.
Min. Bias.	257.8	25.4
60-93%	14.5	4.0

Table 7.1: Values of N_{COLL} from Glauber Monte Carlo simulations [26][24].
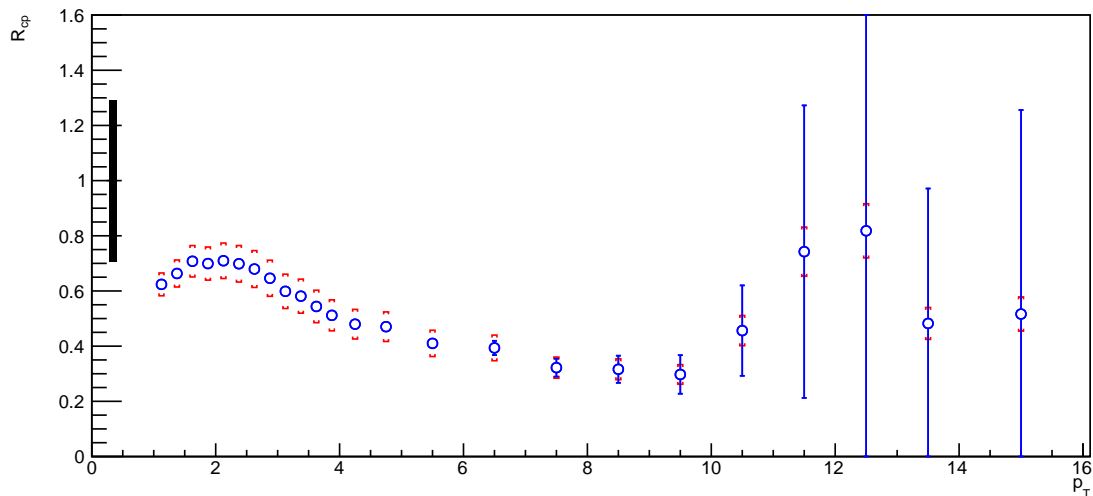
Figure 7-1: Work in progress ratio of the fully corrected charged hadron invariant yield in minimum bias events to the fully corrected yield in events from the 60-93% centrality class. Each spectrum has been scaled by the number of binary collisions N_{COLL} for its centrality class.

7.1 R_{CP}

To measure the modification of the p_T spectrum of charged hadrons in minimum bias collisions compared to peripheral collisions the R_{CP} is measured. The R_{CP} is defined as the ratio of the spectrum in minimum bias to the spectrum in peripheral collisions. Each spectrum is scaled by the inverse of the number of events in its centrality class. The spectra are also scaled by the estimated number of binary nucleon-nucleon collisions in each centrality class (N_{COLL}). By normalizing by an estimate of the number of binary nucleon-nucleon collisions, observables from differently sized collision systems can be compared side-by-side. The values of N_{COLL} used in this analysis are shown in table 7.1 and are from Glauber Monte Carlo

simulations[26][24]. A Glauber Monte Carlo simulates nucleus-nucleus collisions as a chain of causally separate nucleon-nucleon collisions[24]. The measured R_{CP} is plotted in figure 7-1. Statistical errors are shown as blue error bars. Systematic uncertainties are shown as red error bars and are mainly associated with uncertainties from the bootstrapped efficiency calculation described in the previous section. The uncertainties on the bootstrapped efficiency come primarily from the fits to ratios to the published charged hadron spectra. These are provided in table 6.1. Whereas the largest systematic uncertainties on the spectra themselves come from the smearing due to momentum resolution, these cancel when dividing the central spectrum by the peripheral.

Many sources of systematic error present in the measurement of the charged hadron spectra are not present in the measurement of R_{CP}. This holds for any error which has the same magnitude in minimum bias as in peripheral (60-93%). This is true for the momentum scale uncertainty. There is an overall p_T and centrality independent scale uncertainty inherent in the drift chamber's measurement of momentum. As it is the same magnitude in minimum bias as in peripheral, it cancels out in the calculation of the R_{CP}. This also applies to the detector acceptance, which is unchanged between minimum bias and peripheral and therefore is not included in the systematic error on R_{CP}. Since the entire curve is scaled by the ratio of the number of binary nucleon collisions, there exists an overall normalization uncertainty associated with the use of the Glauber Monte Carlo simulation to estimate N_{COLL}[26][24]. This uncertainty is shown as the black band around unity. It can be seen that the R_{CP} appears to be enhanced around $p_T = 2$ GeV/c and decreases until $p_T = 6$ GeV/c where it plateaus. Between $p_T = 6$ and $p_T = 10$ GeV/c the data is consistent with a flat R_{CP} and R_{CP} would appear to be constant. This is consistent with previous results. Unfortunately, limited statistics in the peripheral class preclude a definite conclusion about the shape above $p_T = 10$ GeV/c.

Chapter 8

Conclusion

In heavy ion collisions at high enough energies, a quark-gluon plasma may form. The quark-gluon plasma is a thermalized state of deconfined quarks and gluons. The properties of the quark-gluon plasma can be explored by identifying and measuring the properties of particles produced during the collision.

Of especial interest to this analysis are hard probes, products of hard scatterings of constituent partons occurring early on in the collision and which manifest themselves later as high-p_T particles. These hard probes must traverse the strongly interacting quark-gluon plasma and in doing so they lose energy and momentum. Energy loss primarily occurs through the process of gluon Bremsstrahlung. As the parton travels through the medium it scatters off color charges, inducing gluonic Bremsstrahlung and resulting in a loss of energy. By measuring the modification of the spectrum of high p_T particles, information about the color charge density can be inferred[6].

The spectrum of charged hadrons in Au+Au collisions at $\sqrt{s_{NN}} = 200$ GeV has been measured up to $p_T = 26$ GeV/c. Before the installation of the silicon vertex tracker upgrade, the spectrum of charged hadrons was limited to $p_T < 10$ GeV/c. This limitation was due to the spectrum being dominated by off-vertex background particles such as photon

conversions and secondary products from weak decays. The silicon vertex detector rejects this background, by only selecting tracks which originate close to the collision vertex and by cutting on a track's distance of closest approach. Cutting on distance of closest approach allows the spectrum to be measured out to high p_T, with a very large signal to background ratio. The signal to background ratio has been estimated to reach unity only above a transverse momentum of 49 GeV/c although statistics limited our measurement to 26 GeV/c.

Ultimately, measuring the charged hadron spectrum at high p_T provides insight into the energy loss mechanisms in the quark-gluon plasma. Energy loss can be observed by measuring the modification of the p_T spectrum with respect to heavy ion collisions in which there is a low likelihood of a quark-gluon plasma forming. This was done by measuring R_{CP}, the ratio of the charged hadron yield from minimum bias events to the yield in peripheral events scaled by the estimated number of binary collisions N_{COLL}. At intermediate transverse momentum, $6 < p_T < 10$, R_{CP} appears to be constant. This is consistent with previous measurements as well as several theory predictions. It has also been shown, by improving background recjection with the silicon vertex detector, the suppression of charged hadrons can be measured to very high p_T, however a higher statistics peripheral measurement is needed to constrain the shape of R_{CP} above $p_T = 10$ GeV/c.

Bibliography

[1] A. Adare et al. Suppression pattern of neutral pions at high transverse momentum in Au+Au collisions at $\sqrt{s_{NN}} = 200$ GeV and constraints on medium transport coefficients. *Phys. Rev. Lett.*, 101:232301, 2008.

[2] A. Adare et al. Neutral pion production with respect to centrality and reaction plane in Au+Au collisions at $\sqrt{s_{NN}}$=200 GeV. *Phys. Rev.*, C87(3):034911, 2013.

[3] A. Adare et al. An Upgrade Proposal from the PHENIX Collaboration. 2015.

[4] A. Adare et al. Single electron yields from semileptonic charm and bottom hadron decays in Au+Au collisions at $\sqrt{s_{NN}} = 200$ GeV. *Phys. Rev.*, C93(3):034904, 2016.

[5] K. Adcox et al. PHENIX central arm tracking detectors. *Nucl. Instrum. Meth.*, A499:489–507, 2003.

[6] K. Adcox et al. Formation of dense partonic matter in relativistic nucleus-nucleus collisions at RHIC: Experimental evaluation by the PHENIX collaboration. *Nucl. Phys.*, A757:184–283, 2005.

[7] S. S. Adler et al. Suppressed π^0 production at large transverse momentum in central Au+ Au collisions at $\sqrt{s_{NN}} = 200$ GeV. *Phys. Rev. Lett.*, 91:072301, 2003.

[8] S.S. Adler et al. High p_T charged hadron suppression in Au + Au collisions at $\sqrt{s}_{NN} = 200$ GeV. *Phys.Rev.*, C69:034910, 2004.

[9] S.S. Adler et al. Identified charged particle spectra and yields in Au+Au collisions at $\sqrt{s}_{NN} = 200$ GeV. *Phys.Rev.*, C69:034909, 2004.

[10] Y. Akiba. Estimate of fake rate in external silicon tracker, 1-2015. Internal PHENIX presentation.

[11] M. Allen et al. PHENIX inner detectors. *Nucl. Instrum. Meth.*, A499:549–559, 2003.

[12] L. Aphecetche et al. PHENIX calorimeter. *Nucl. Instrum. Meth.*, A499:521–536, 2003.

[13] Peter Brockway Arnold, Guy D. Moore, and Laurence G. Yaffe. Photon and gluon emission in relativistic plasmas. *JHEP*, 06:030, 2002.

[14] S. H. Aronson et al. PHENIX magnet system. *Nucl. Instrum. Meth.*, A499:480–488, 2003.

[15] R Averbeck. Particle Identification by Correlating Time-of-flight and Momentum Measurement, 1-2001. PHENIX internal analysis note 37.

[16] Steffen A. Bass, Charles Gale, Abhijit Majumder, Chiho Nonaka, Guang-You Qin, Thorsten Renk, and Jorg Ruppert. Systematic Comparison of Jet Energy-Loss Schemes in a realistic hydrodynamic medium. *Phys. Rev.*, C79:024901, 2009.

[17] S. Butsyk. PHENIX Drift Chamber operation principles. `http://www.phenix.bnl.gov/phenix/WWW/intro/detectors/focus/focus_dch.pdf`, 1-2003. PHENIX seminar talk. [Accessed: 2016-03-26].

[18] K. Adcox et al. Phenix detector overview. *Nuclear Instruments and Methods in Physics Research A*, 499:469–479, 2003.

[19] T. Hachiya. PHENIX Silicon Vertex Tracker (VTX). `http://www.phenix.bnl.gov/phenix/WWW/intro/detectors/focus/focus_vtx.pdf`, 2-2011. PHENIX seminar talk. [Accessed: 2016-03-26].

[20] T Hachiya. Fitting of SvxCentralTrackReco, 3-2016. PHENIX internal technical documentation.

[21] M. Harrison, T. Ludham, and S. Ozaki. Rhic project overview. *Nuclear Instruments and Methods in Physics Research A*, 499:235–244, 2003.

[22] A. Majumder, R. J. Fries, and Berndt Muller. Photon bremsstrahlung and diffusive broadening of a hard jet. *Phys. Rev.*, C77:065209, 2008.

[23] A. Majumder and C. Shen. Suppression of the High p_T Charged Hadron R_{AA} at the LHC. *Phys. Rev. Lett.*, 109:202301, 2012.

[24] Michael L. Miller, Klaus Reygers, Stephen J. Sanders, and Peter Steinberg. Glauber modeling in high energy nuclear collisions. *Ann. Rev. Nucl. Part. Sci.*, 57:205–243, 2007.

[25] K. A. Olive et al. Review of Particle Physics. *Chin. Phys.*, C38:090001, 2014.

[26] K Reygers. Glauber Monte Carlo Calculations, 12-2005. PHENIX internal technical documentation.

[27] H. Buesching [PHENIX Collaboration] S. Bathe. Parameterization of the final Run3 π_0 cross section in $p + p$. PHENIX internal analysis note. 2005.

[28] Carlos A. Salgado and Urs Achim Wiedemann. Calculating quenching weights. *Phys. Rev.*, D68:014008, 2003.

[29] Maya Shimomura. High-p(T) pi0, eta, identified and inclusive charged hadron spectra from PHENIX. *Nucl. Phys.*, A774:457–460, 2006.

[30] H.W. van Hecke. PHENIX Photos & Drawings. `https://www.phenix.bnl.gov/WWW/run/drawing/phenix_quartercut.png`. [Accessed: 2016-04-23].

[31] Urs Achim Wiedemann. Transverse dynamics of hard partons in nuclear media and the QCD dipole. *Nucl. Phys.*, B582:409–450, 2000.